2011

Transmission-Line Metamaterial Design of an Embedded Line Source in a Ground Recess

Caglar D. Emiroglu
University of Massachusetts Amherst

TRANSMISSION-LINE METAMATERIAL DESIGN OF AN EMBEDDED LINE SOURCE IN A GROUND RECESS

A Thesis Presented

by

CAGLAR D. EMIROGLU

Submitted to the Graduate School of the
University of Massachusetts Amherst in partial fulfillment
of the requirements for the degree of

MASTER OF SCIENCE IN ELECTRICAL AND COMPUTER ENGINEERING

May 2011

Electrical and Computer Engineering

TRANSMISSION-LINE METAMATERIAL DESIGN OF AN EMBEDDED LINE SOURCE IN A GROUND RECESS

A Thesis Presented

by

CAGLAR D. EMIROGLU

Approved as to style and content by:

Do-Hoon Kwon, Chair

Ramakrishna Janaswamy, Member

Marinos N. Vouvakis, Member

C. V. Hollot, Department Head
Electrical and Computer Engineering

To my parents.

ABSTRACT

TRANSMISSION-LINE METAMATERIAL DESIGN OF AN EMBEDDED LINE SOURCE IN A GROUND RECESS

MAY 2011

CAGLAR D. EMIROGLU

B.Sc., MIDDLE EAST TECHNICAL UNIVERSITY

M.S.E.C.E., UNIVERSITY OF MASSACHUSETTS AMHERST

Directed by: Professor Do-Hoon Kwon

A transmission-line metamaterial design of a material-embedded electric line source radiating inside a ground recess is investigated. The media embedding the recessed line source are designed such that the embedded current creates the same radiation pattern as a line source over a flat conducting ground plane. Transmission-line metamaterial unit cell designs for the embedding media obtained from the transformation electromagnetics design technique are shown. The metamaterial design of the overall embedded source configuration is numerically tested using circuit simulations. It is shown that the embedded-source design creates the same radiation characteristics as the line source above a flat ground plane at the design frequency.

TABLE OF CONTENTS

Page

LIST OF TABLES

Table **Page**

LIST OF FIGURES

Figure **Page**

CHAPTER 1

INTRODUCTION

Metamaterials are artificial structures that can be constructed to have unconventional electromagnetic properties which may not be commonly found in nature. They are designed to interact with and control electromagnetic waves. Unusual properties of metamaterials have allowed novel applications, concepts and devices.

This thesis work presents a transmission-line (TL) metamaterial design of an embedded line source radiating inside a ground recess. The media embedding the recessed line source is designed such that the embedded current yields the same far-field radiation characteristics as a line source over a flat conducting ground plane. In this chapter, the background needed to understand the purpose of the project and the motivation for studying this problem are presented. The material properties of the embedding media are presented in Chapter 2. In Chapter 3, the non-orthogonal transmission line unit cell structure is introduced and its characteristics are numerically demonstrated. Two-dimensional (2D) TL metamaterial design is discussed in Chapter 4 along with the periodic unit cells. The overall embedded source configuration is numerically tested using circuit simulations and numerical analysis results are presented in Chapter 5.

1.1 Background

The transformation optics/electromagnetics technique [1] allows designing novel electromagnetic and optical devices that feature unconventional wave-material interaction properties. The theory is based on the form-invariant nature of Maxwell's equations under spatial coordinate transformations [2]. Utilizing this method, various device designs have

been introduced following the invisibility cloak proposed in [1] and [3]. Embedded transformations were introduced in [4], generalizing the technique to coordinate transformations possessing discontinuities along device boundaries. Overviews of the coordinate transformation based device designs are available in [5, 6]. In addition, a negative-index material (NIM) superlens or the "perfect lens" [7] was interpreted in [8] as a device that realizes a coordinate transformation involving a negative slope between coordinates.

Similar to the change in the material parameters as a result of a coordinate transformation in space, a change in the source distribution results with a transformation on a volume containing sources. The behavior of line sources and surface currents under coordinate transformations were investigated in [9]. In [10–12], source transformations were applied to different array structures. In [13], a material-embedded monopole antenna inside a ground recess was designed such that the embedded antenna creates the same far-zone radiation pattern as the same monopole placed over a flat conducting ground plane. The embedded configuration is flush with the surrounding ground plane and there is no physical structure above the ground plane. It is capable of radiating vertically polarized fields with a pattern maximum in the horizon on the ground plane.

1.2 Motivation

The 2D TL metamaterial design approach [14, 15] has been useful in realizing coordinate transformation based designs. The theory is a widely used analysis and design tool for conventional right/left-handed metamaterials which can be realized using loaded coaxial or microstrip lines. In [16], the TL approach was used to design and simulate a cylindrical invisibility cloak. Loaded TL networks constructed with lumped elements were utilized for the simulation. In [17], a method for designing TL metamaterials with arbitrary material tensors was proposed. A TL unit cell topology that can represent full-tensor material parameters was presented and demonstrated. In contrast, this study utilizes a different unit-cell topology based on the coordinate transformation technique. The topology uses the

skewness of a unit cell's branches instead of adding additional branches intersecting at a node. This topology enables a direct extension to a three-dimensional (3D) adaptation of the implementation.

In this study, a TL metamaterial design for the 2D version of the material-embedded antenna introduced in [13] is investigated. A coordinate transformation maps a 2D line source above a flat ground plane into one embedded in transformation-derived media inside a ground recess such that the embedded-recessed line source has the same far-field radiation characteristics as the original configuration. The TL metamaterial design method is utilized to obtain a 2D circuit network for lumped circuit implementations.

Cavity-backed antennas have been widely used and analyzed in the past, and numerous studies have been reported in the literature. A cavity-backed spiral antenna design was presented in [18]. In [19–21], characteristics of several cavity-backed slot antenna designs were investigated. In practical applications, one of the drawbacks of slot antennas is the bidirectional radiation characteristic. In [22,23], a cavity was used to eliminate the backside radiation of slot antennas. In contrast, in this study, it is targeted to embed a line source inside a recess below the ground plane, without distorting the far-field radiation pattern. In other words, the recess serves as a nest for the embedding media and the line source.

Motivation of the overall research is to design a material-embedded monopole antenna that radiates vertically polarized fields with a pattern maximum in the horizon on the ground plane, as numerically investigated in [13]. This configuration will be completely flush with the surrounding ground plane, having no physical component above it. This advantage of the setup will be more significant when low profile antennas are needed at low frequencies, where antenna dimensions are physically large.

This thesis work is the first step towards the objective, where a design of the 2D TL metamaterial radiation configuration is investigated to validate the approach. Future work includes an extension of the embedded line source configuration from the TL metamaterial

design to a resonator-based counterpart. Then, design and implementation of the embedded 3D monopole setup using resonant inclusion-based metamaterials will be the next step.

CHAPTER 2

EMBEDDED LINE SOURCE DESIGN BASED ON COORDINATE TRANSFORMATION

In this chapter, coordinate transformation design of the problem will be presented. Material parameters of the embedding media are calculated.

Consider a 2D line source along $+\hat{z}$ direction radiating at $(x, y) = (0, s)$ in free space above a perfectly conducting $x-z$ ground plane in the Cartesian (x, y, z) coordinate system as shown in Figure 2.1(a). It is desired that a line source and embedding media be arranged inside a ground recess, such that the new arrangement has the same far-zone radiation pattern as the original configuration at the operating frequency. The resulting radiation configuration is completely flush with the surrounding ground plane and there is no physical structure above the $x - z$ plane. This is a 2D variant of the coordinate transformation design of an embedded monopole in a ground recess [13]. Figure 2.1(b) depicts the desired configuration.

A coordinate transformation from the original (virtual) to the transformed (physical) systems specifies the material parameter values of the embedding region. We choose to transform only the coordinate normal to the ground plane; the region bounded by the dashed contour and the ground plane in Figure 2.1(a) is folded below the ground plane in Figure 2.1(b). The transformation from y to y' is kept continuous along $y' = 0$ to ensure the interface reflectionless. The following transformation can be defined:

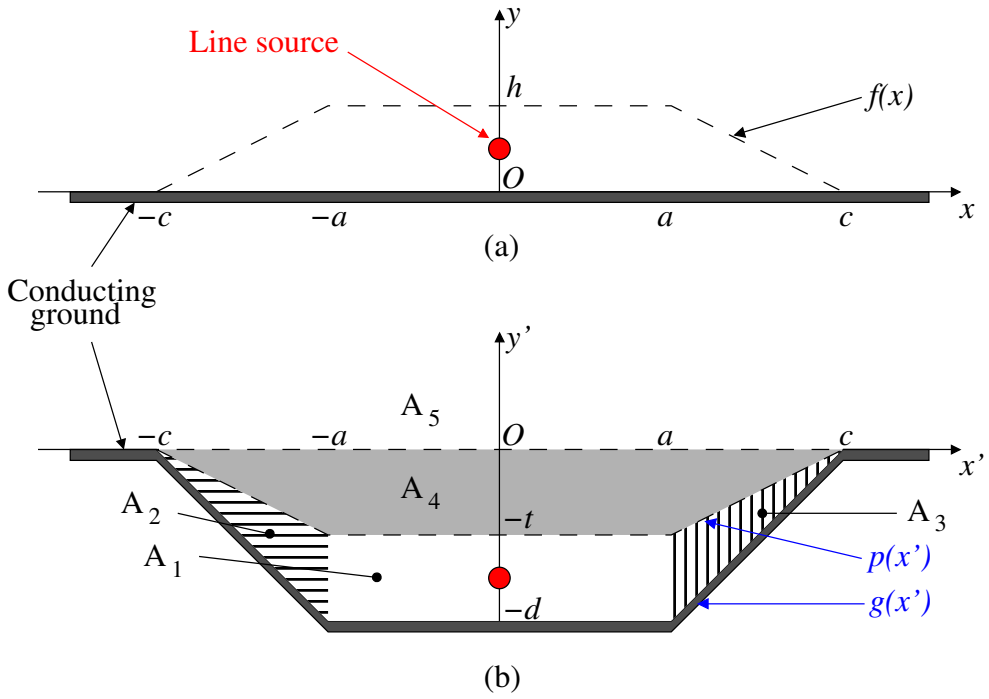

Figure 2.1. The coordinate transformation between the original (virtual) and embedded (physical) radiation configurations. (a) Original configuration. (b) Embedded configuration.

$$x = x', z = z',$$

$$y = \begin{cases} y', & y' \geq 0 \\ \frac{f(x)}{p(x')} y', & p(x') \leq y' < 0 \\ \frac{f(x)}{p(x')-g(x')}[y' - g(x')], & g(x') \leq y' < p(x') \end{cases} . \tag{2.1}$$

One first finds the Jacobian matrix of the transformation $\mathbf{A} = \partial(x', y', z')/\partial(x, y, z)$ and then computes the relative permittivity and permeability tensors from $\mathbf{A}$ for regions A_1, A_2, A_3 and A_4 [24]. In Cartesian bases, non-zero elements of 3×3 tensors are found to be

$$\mu'_{x'x'} = \epsilon'_{z'z'} = \frac{h}{d-t},\ \mu'_{y'y'} = \frac{d-t}{h} \text{ in } A_1, \tag{2.2}$$

$$\mu'_{x'x'} = \epsilon'_{z'z'} = \frac{h}{d-t},\ \mu'_{x'y'} = \mu'_{y'x'} = \frac{hd}{(a-c)(d-t)},$$

$$\mu'_{y'y'} = \frac{d-t}{h} + \frac{hd^2}{(c-a)^2(d-t)} \text{ in } A_2, \tag{2.3}$$

$$\mu'_{x'x'} = \epsilon'_{z'z'} = \frac{h}{d-t},\ \mu'_{x'y'} = \mu'_{y'x'} = \frac{hd}{(c-a)(d-t)},$$

$$\mu'_{y'y'} = \frac{d-t}{h} + \frac{hd^2}{(c-a)^2(d-t)} \text{ in } A_3, \tag{2.4}$$

$$\mu'_{x'x'} = \epsilon'_{z'z'} = -\frac{h}{t},\ \mu'_{y'y'} = -\frac{t}{h} \text{ in } A_4. \tag{2.5}$$

We now remove primes in (2.2)–(2.5) to interpret them as medium parameters in the original space.

Of particular interest is the choice $h = t = d/2$, with which A_1 and A_4 become isotropic media, A_1 is free space and A_4 is a negative-index material (NIM) with $\epsilon = \mu = -1$. For the lateral dimension, choosing $a = c/2 = d$, yields following anisotropic tensor parameters:

$$\boldsymbol{\epsilon} = \boldsymbol{\mu} = \begin{bmatrix} 1 & \mp 1 & 0 \\ \mp 1 & 2 & 0 \\ 0 & 0 & 1 \end{bmatrix} \tag{2.6}$$

for the remaining regions A_2 and A_3. It is noted that all constituent blocks A_1, A_2, A_3, and A_4 are homogeneous. The free space region in $y > 0$ is denoted as A_5.

The radiation characteristics of an embedded line source are numerically investigated using COMSOL Multiphysics which is a commercial full-wave analysis tool based on the finite-element technique. At the design frequency, a line source along the $+\hat{z}$ direction is placed $\lambda_0/4$ above the ground plane at $(x, y) = (0, 0.25\lambda_0)$ for the original and at $(0, -0.75\lambda_0)$ for the embedded configurations. Dimensional parameters of the ground recess were chosen to be $a = d = c/2 = 2h = 2t = \lambda_0$. Snapshots of the electric field distributions are compared in Figure 2.2 for two configurations. It can be observed that the

same field distribution is reproduced away from the immediate neighborhood of the boundary at $y = 0$. The high field values along the horizontal NIM boundaries are associated with surface-mode plasmon resonances.

In principle, the design relies on the same physics as a NIM superlens [7], with two major distinctions. First, the horizontal dimension of the NIM lens is finite and the associated truncation effect is compensated by the impedance-matching regions A_2 and A_3. Second, no extreme accuracy is required for the effective medium parameters in practical antenna applications [13], unlike in the sub-diffraction-limit near-field lensing applications [25].

In comparison, we consider an embedded line source inside a rectangular ground recess in order to stress the function of the impedance-matching regions. This configuration is shown in Figure 2.3(a), where a line source is placed at $(x, y) = (0, -0.75\lambda_0)$. Dimensional parameters for the recess are chosen to be $a = d = 2t = \lambda_0$. The NIM slab with $\epsilon = \mu = -1$ is present between $y = 0$ and $y = -0.5\lambda_0$. A snapshot of the electric field distribution is provided in Figure 2.3(b). This distribution clearly shows significant distortion compared to Figure 2.2(b) due to the truncation effect associated to the finite horizontal dimension of the NIM lens region.

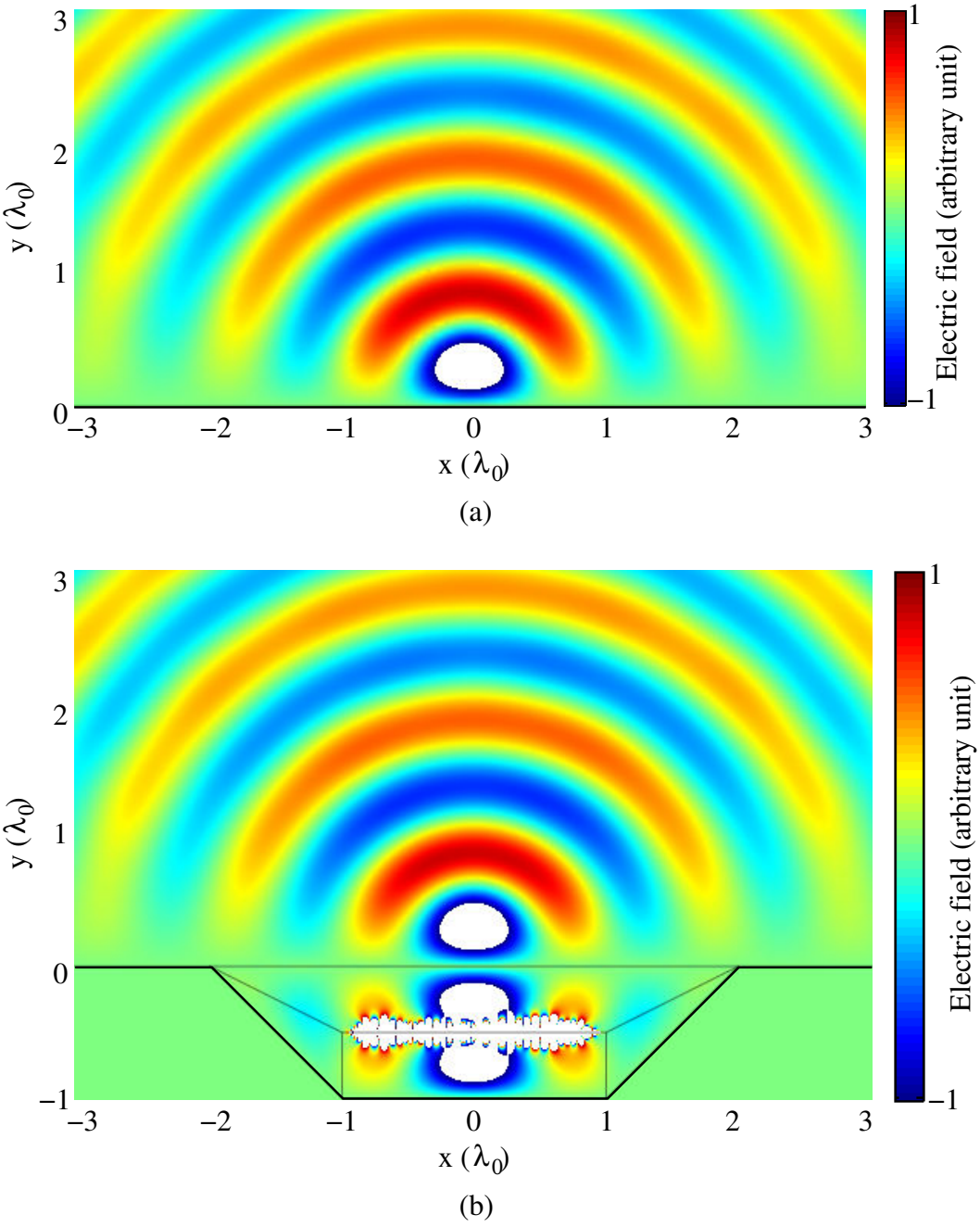

Figure 2.2. Snapshots of the electric field. (a) Original configuration. (b) Embedded configuration.

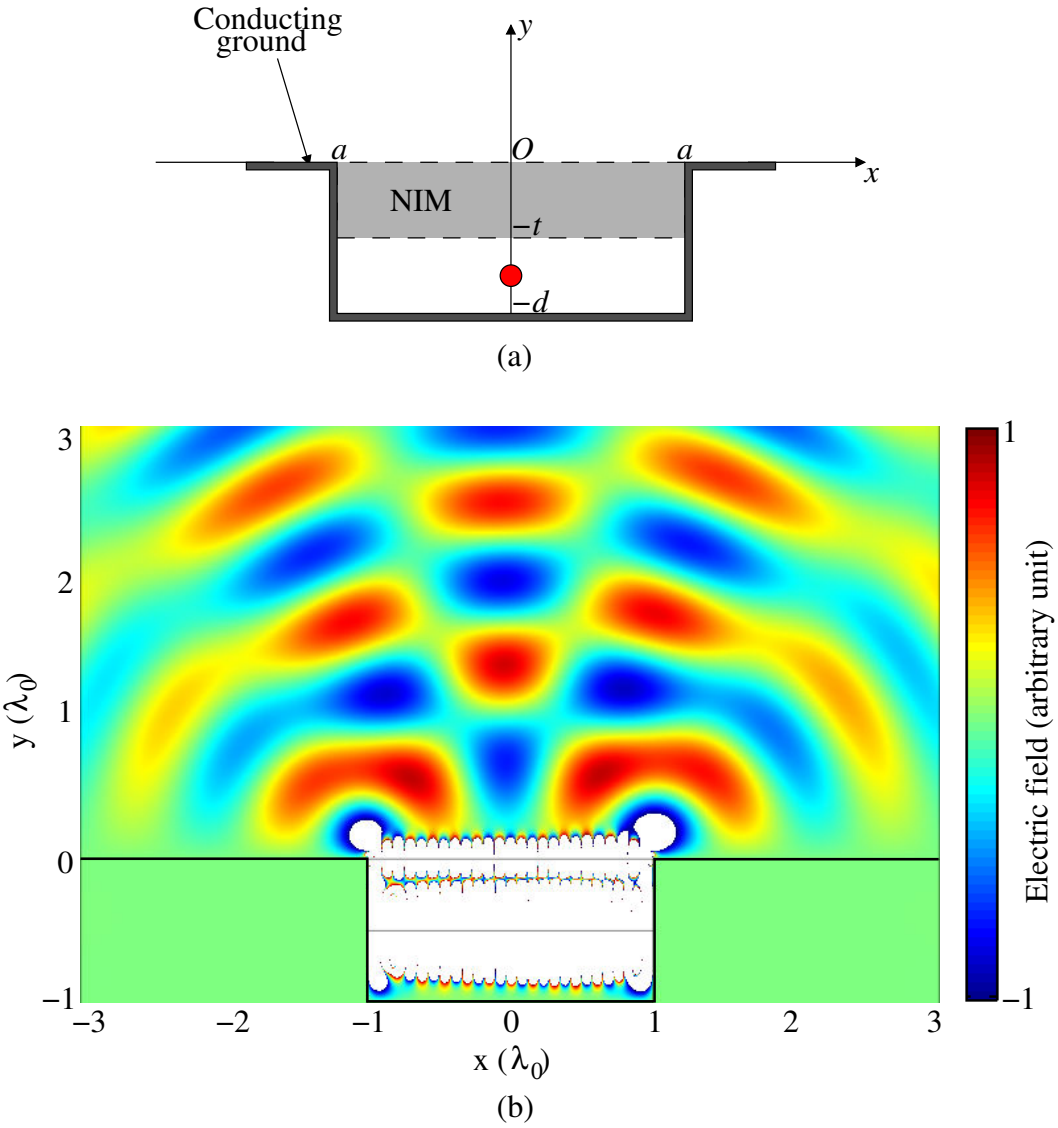

Figure 2.3. Line source inside a rectangular ground recess. (a) The configuration. (b) A snapshot of the electric field.

CHAPTER 3

NON-ORTHOGONAL GRIDS IN 2D TL METAMATERIALS

The 2D effective medium design in Chapter 2 can be implemented in TL metamaterials using periodic unit cells. Several design approaches have been reported regarding the implementation of regions that possess anisotropic material parameters. This chapter summarizes the design of non-orthogonal TL metamaterial grid unit cell introduced in [26] for realizing arbitrary full-tensor medium parameters.

3.1 The Non-Orthogonal Grid Unit Cell

The shunt node configuration for 2D TL networks is used to model 2D electromagnetic fields in the TE polarization [27]. A non-orthogonal grid TL metamaterial unit cell is illustrated in Figure 3.1. Total series impedances along the two branches are Z_1 and Z_2, and a shunt admittance Y is connected between the junction of the series branches and the ground as shown in Figure 3.1. Voltages and currents at the four nodes are also indicated. The advantage of this unit cell over the conventional unit cell approaches [14] is that both branches are allowed to run in fixed, but arbitrary directions. In the non-orthogonal (q_1, q_2, q_3) coordinate system shown in Figure 3.2, q_1 and q_2 axes are aligned with the series branches. The unit vector sets $\hat{q}_1, \hat{q}_2, \hat{q}_3$ built along the coordinate axes and $\hat{q}^1, \hat{q}^2, \hat{q}^3$ built normal to coordinate surfaces are also defined, where $\hat{q}_3 = \hat{q}^3 = \hat{z}$. The lengths of the series branches are p_1 and p_2, and the height of the shunt branch is p_3. The geometrical arrangement of immittances constitutes a non-orthogonal grid unit cell or a parallelogram unit cell as indicated with a dashed-line in Figure 3.2.

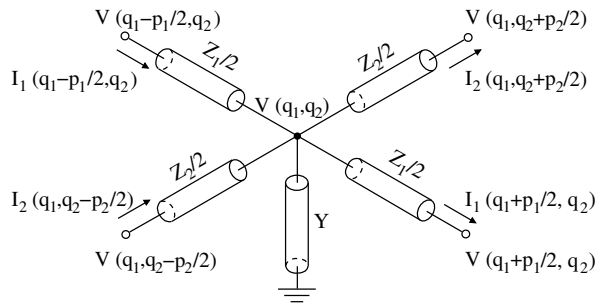

Figure 3.1. A perspective view of the non-orthogonal grid TL metamaterial unit cell.

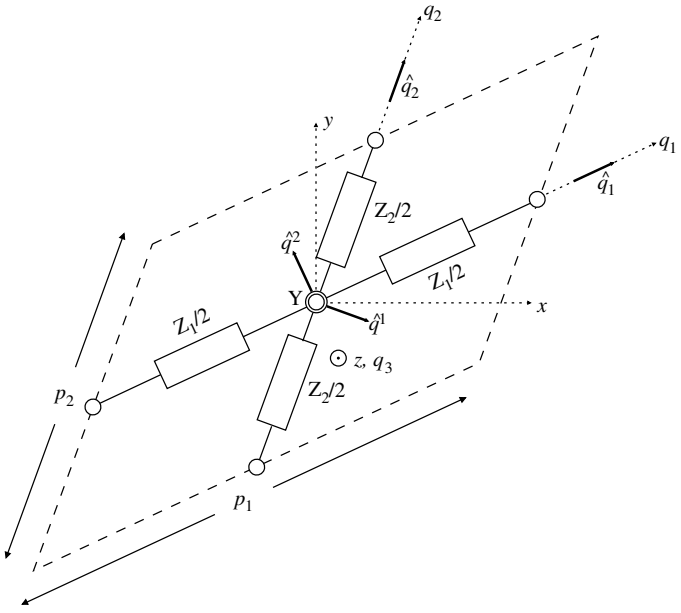

Figure 3.2. Top view of the non-orthogonal grid TL metamaterial unit cell.

The effective medium parameters represented by the non-orthogonal unit cell can be found by establishing an isomorphism between Kirchoff's circuital laws and 2D Maxwell's equations in the TE polarization. In the limit $p_1, p_2 \to 0$, application of Kirchoff's voltage law along the two branches gives

$$\frac{\partial V}{\partial q_1} = -(\hat{q_3} \cdot \hat{q_1} \times \hat{q_2}) Z_1' \left(\frac{I_1}{p_2} \right), \tag{3.1}$$

$$\frac{\partial V}{\partial q_2} = -(\hat{q_3} \cdot \hat{q_1} \times \hat{q_2}) Z_2' \left(\frac{I_2}{p_1} \right). \tag{3.2}$$

Kirchoff's current law applied at the junction results in

$$\frac{\partial}{\partial q_1}\left(\frac{I_1}{p_2}\right)+\frac{\partial}{\partial q_2}\left(\frac{I_2}{p_1}\right)=-(\hat{q_3}\cdot\hat{q_1}\times\hat{q_2})Y'V. \tag{3.3}$$

Primed immittances in (3.1)–(3.3) are per-unit-length quantities of the unprimed counterparts for the medium being modeled. For TE-polarized 2D electromagnetic fields $\mathbf{E}$ ($E_3=\hat{q_3}\cdot\mathbf{E}$) and $\mathbf{H}$ ($H_1=\hat{q_1}\cdot\mathbf{H}, H_2=\hat{q_2}\cdot\mathbf{H}$), the source-free time-harmonic Maxwell's equations written in the (q_1,q_2,q_3) system take the same form as in the Cartesian system, i.e.

$$\nabla\times\mathbf{E}=-j\omega\mu_0\boldsymbol{\mu}\mathbf{H}, \tag{3.4}$$

$$\nabla\times\mathbf{H}=j\omega\epsilon_0\boldsymbol{\epsilon}\mathbf{E}, \tag{3.5}$$

due to the form-invariant nature of Maxwell's equations [2]. In (3.4)–(3.5), $\boldsymbol{\mu}$ and $\boldsymbol{\epsilon}$ are permeability and permittivity sensors relative to free space. The network equations (3.1)–(3.3) and Maxwell's equations (3.4)–(3.5) are isomorphic with the following substitutions

$$E_3\to-\frac{V}{p_3},\quad H_1\to-\frac{I_2}{p_1},\quad H_2\to\frac{I_1}{p_2} \tag{3.6}$$

for field quantities and

$$\boldsymbol{\epsilon}\to\hat{q_3}\hat{q_3}\frac{\hat{q_3}\cdot\hat{q_1}\times\hat{q_2}}{j\omega\epsilon_0}Y', \tag{3.7}$$

$$\boldsymbol{\mu}\to\frac{\hat{q_3}\cdot\hat{q_1}\times\hat{q_2}}{j\omega\mu_0}(\hat{q_1}\hat{q_1}Z_2'+\hat{q_2}\hat{q_2}Z_1') \tag{3.8}$$

for medium parameters. Therefore, expressed in the (q_1,q_2,q_3) system, the effective medium parameters represented by the non-orthogonal grid are

$$\begin{bmatrix}\mu_{11}&0\\0&\mu_{22}\end{bmatrix}=\frac{\hat{q_3}\cdot\hat{q_1}\times\hat{q_2}}{j\omega\mu_0}\begin{bmatrix}Z_2'&0\\0&Z_1'\end{bmatrix},\quad \epsilon_{33}=\frac{\hat{q_3}\cdot\hat{q_1}\times\hat{q_2}}{j\omega\epsilon_0}Y', \tag{3.9}$$

where primed immittances in (3.9) are per-unit-length quantities of the unprimed counterparts for the medium being modeled.

3.2 Coordinate Transformation

In order to utilize the non-orthogonal grid to synthesize anisotropic medium with a full tensor in the Cartesian system, it is of interest to find the relative effective medium parameters (3.9) in the (x, y, z) system, which are denoted by

$$\begin{bmatrix} \mu_{xx} & \mu_{xy} \\ \mu_{yx} & \mu_{yy} \end{bmatrix}, \quad \epsilon_{zz}. \tag{3.10}$$

Restricting our attention to reciprocal media, we impose the condition $\mu_{yx} = \mu_{xy}$ in (3.10). Consider a coordinate transformation from (q_1, q_2, q_3) to (x, y, z). The Jacobian matrix $\mathbf{A} = \partial(x, y, z)/\partial(q_1, q_2, q_3)$ of the transformation is equal to

$$\mathbf{A} = \begin{bmatrix} \hat{x} \cdot \hat{q}_1 & \hat{x} \cdot \hat{q}_2 & \hat{x} \cdot \hat{q}_3 \\ \hat{y} \cdot \hat{q}_1 & \hat{y} \cdot \hat{q}_2 & \hat{y} \cdot \hat{q}_3 \\ \hat{z} \cdot \hat{q}_1 & \hat{z} \cdot \hat{q}_2 & \hat{z} \cdot \hat{q}_3 \end{bmatrix} = \begin{bmatrix} \hat{q}_1 & \hat{q}_2 & \hat{q}_3 \end{bmatrix}, \tag{3.11}$$

where $\hat{q}_1, \hat{q}_2, \hat{q}_3$ are written as column vectors in Cartesian components. The medium tensor parameters in the (x, y, z) system are then expressed by $\mathbf{A}\epsilon\mathbf{A}^T/|\mathbf{A}|$ and $\mathbf{A}\mu\mathbf{A}^T/|\mathbf{A}|$ [24]. Let $\hat{q}_1$ and $\hat{q}_2$ in Figure 3.2 make angles ϕ_1 and ϕ_2 from the $+x$ direction in the $x - y$ plane such that

$$\hat{q}_1 = \hat{x}\cos\phi_1 + \hat{y}\sin\phi_1, \quad \hat{q}_2 = \hat{x}\cos\phi_2 + \hat{y}\sin\phi_2. \tag{3.12}$$

One finds the medium parameters in the (x, y, z) system to be

$$\mu_{xx} = \frac{\mu_{11}\cos^2\phi_1 + \mu_{22}\cos^2\phi_2}{\sin(\phi_2 - \phi_1)}, \tag{3.13}$$

$$\mu_{yx} = \mu_{xy} = \frac{\mu_{11}\sin\phi_1\cos\phi_1 + \mu_{22}\sin\phi_2\cos\phi_2}{\sin(\phi_2 - \phi_1)}, \tag{3.14}$$

$$\mu_{yy} = \frac{\mu_{11}\sin^2\phi_1 + \mu_{22}\sin^2\phi_2}{\sin(\phi_2 - \phi_1)}, \tag{3.15}$$

$$\epsilon_{zz} = \frac{\epsilon_{33}}{\sin(\phi_2 - \phi_1)}. \tag{3.16}$$

Useful inverse relations can be obtained from (3.13)–(3.16):

$$\mu_{11} = \frac{\mu_{xx}\sin^2\phi_2 - \mu_{yy}\cos^2\phi_2}{\sin(\phi_1 + \phi_2)}, \tag{3.17}$$

$$\mu_{22} = -\frac{\mu_{xx}\sin^2\phi_1 - \mu_{yy}\cos^2\phi_1}{\sin(\phi_1 + \phi_2)}, \tag{3.18}$$

$$\epsilon_{33} = \epsilon_{zz}\sin(\phi_2 - \phi_1), \tag{3.19}$$

$$\tan\phi_1 = -\frac{\mu_{yy}\cos\phi_2 - \mu_{xy}\sin\phi_2}{\mu_{xx}\sin\phi_2 - \mu_{xy}\cos\phi_2}. \tag{3.20}$$

3.3 Design Procedure

In the $x - y$ plane, three independent medium parameters μ_{xx}, μ_{xy}, and μ_{yy} in (3.10) need to be synthesized in a typical design problem. This requires three independent design parameters for a unit cell. In comparison, the non-orthogonal unit cell in Figure 3.2 has four design parameters in the $x - y$ plane, namely Z_1, Z_2, ϕ_1, and ϕ_2. Design flexibility is achieved with this one extra degree of freedom. For example, one grid direction can be chosen in an arbitrary direction. If there is an interface between two media, one grid can run always along the interface. The other three parameter values are then uniquely determined to synthesize a given arbitrary full-tensor parameter.

In a design problem for full-tensor (3.10) material parameters, the following design procedure can be taken. First, determine one grid angle, e.g. ϕ_1, in a preferred direction. Second, determine the angle ϕ_2 according to (3.20). Finally, two diagonal elements of $\boldsymbol{\mu}$ in the (q_1, q_2, q_3) system are found from (3.17–3.18). The value of ϵ_{33} is found from (3.19).

These medium parameters of the (q_1, q_2, q_3) system determine the immittance values Y' and Z_1', Z_2' in the non-orthogonal grid unit cell via (3.9).

Y and Z_1, Z_2 are equal to [27]

$$Y = Y' \frac{p_1(\hat{q}^2 \cdot \hat{q}_2 p_2)}{p_3} = j\omega\epsilon_0\epsilon_{33}\frac{p_1 p_2}{p_3}, \tag{3.21}$$

$$Z_1 = Z_1' \frac{(\hat{q}^1 \cdot \hat{q}_1 p_1)p_3}{p_2} = j\omega\mu_0\mu_{22}\frac{p_1 p_3}{p_2}, \tag{3.22}$$

$$Z_2 = Z_2' \frac{(\hat{q}^2 \cdot \hat{q}_2 p_2)p_3}{p_1} = j\omega\mu_0\mu_{11}\frac{p_2 p_3}{p_1}. \tag{3.23}$$

These values can be expressed relative to their free-space counterparts:

$$Y_0 = j\omega\epsilon_0\frac{p_1 p_2}{p_3}, \quad Z_{10} = j\omega\mu_0\frac{p_1 p_3}{p_2}, \quad Z_{20} = j\omega\mu_0\frac{p_2 p_3}{p_1}. \tag{3.24}$$

Y_0 and Z_{10}, Z_{20} in (3.24) are the cell immittance values associated with an orthogonal grid corresponding to free space with periods p_1 and p_2 in the $\hat{x}$ and $\hat{y}$ directions, respectively. Via (3.24), (3.21–3.23) can be rewritten as

$$Y = \epsilon_{33} Y_0, \quad Z_1 = \mu_{22} Z_{10}, \quad Z_2 = \mu_{11} Z_{20}. \tag{3.25}$$

We can split the total immittances of (3.25) into host and loading part contributions by defining

$$Y = Y_0 + Y_l, \quad Z_1 = Z_{10} + Z_{1l}, \quad Z_2 = Z_{20} + Z_{2l}. \tag{3.26}$$

In practice, the immittance values Y_0, Z_{10}, Z_{20} may be realized by an unloaded host TL grid and Y_l, Z_{1l}, Z_{2l} may be implemented with lumped load elements. Full-tensor anisotropic medium synthesization with the non-orthogonal unit cell structure is simple, since no additional load elements are needed compared with the conventional orthogonal grid unit cells.

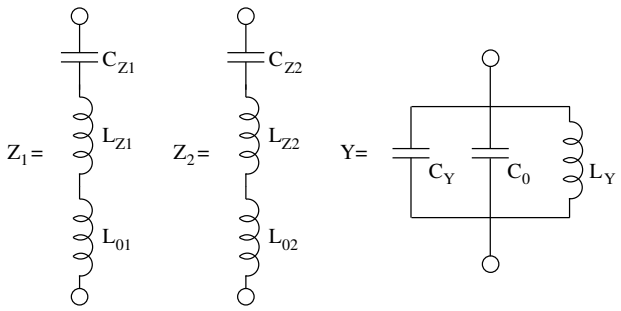

Figure 3.3. Lumped element representations of the unit cell immittances.

3.4 A Numerical Example

To validate the non-orthogonal grid unit cell design for synthesizing full-tensor medium parameters in 2D, a radiation problem by a line source near a linear reflectionless interface between two anisotropic media is investigated. A 2D wave refraction problem that has an exact analytical solution is chosen intentionally, so that a numerical solution from a TL metamaterial circuit network based on non-orthogonal grids can be tested. We will consider lumped circuit elements representations for the immittances Y, Z_1 and Z_2 as illustrated in Figure 3.3. Thus,

$$Y = j\omega C_0 + \frac{1}{j\omega C_Y} + j\omega L_Y, \tag{3.27}$$

$$Z_1 = j\omega L_{01} + \frac{1}{j\omega C_{Z1}} + j\omega L_{Z1}, \tag{3.28}$$

$$Z_2 = j\omega L_{02} + \frac{1}{j\omega C_{Z2}} + j\omega L_{Z2}. \tag{3.29}$$

These choices correspond to the lumped-element version of the composite right/left-handed (CRLH) TL metamaterials [14] and the positive/negative-refractive-index TL metamaterials. Terms in (3.27)–(3.29) correspond to the host TL grid and loading elements.

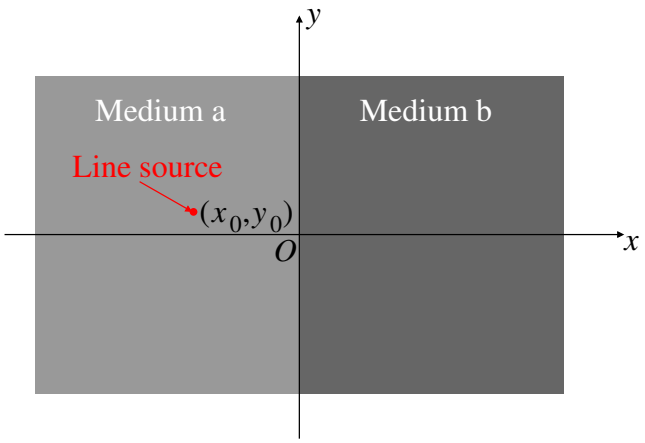

Figure 3.4. Problem configuration of a line source radiating near a linear interface between two homogeneous, anisotropic media.

3.4.1 Line Source Radiation Near a Reflectionless Interface

As illustrated in Figure 3.4, two anisotropic semi-infinite media — medium a and medium b — has a planar boundary in the $y-z$ plane. Quantities associated with either medium is indicated by a superscript 'a' or 'b'. At an angular frequency $\omega = 2\pi f$, an electric line source radiates time-harmonic fields from $(x, y) = (x_0, y_0)$. Two media are based on the following transformation from free space in the (x, y, z) system to the transformed (x', y', z') system:

$$x' = x, \quad y' = \begin{cases} \alpha^a x + y & \text{in } x < 0 \\ \alpha^b x + y & \text{in } x \geq 0 \end{cases}, \quad z' = z. \tag{3.30}$$

Since the transformation (3.30) is continuous at $x = 0$, the interface is reflectionless for any wave — propagating or evanescent. The two parameters in (3.30) are selected to be $\alpha^a = -0.3640$ and $\alpha^b = 0.5774$ with which the tensor metamaterial parameters for the two media are equal to

$$\epsilon^a = \mu^a = \begin{bmatrix} 1 & -0.3640 & 0 \\ -0.3640 & 1.1325 & 0 \\ 0 & 0 & 1 \end{bmatrix}, \tag{3.31}$$

$$\epsilon^b = \mu^b = \begin{bmatrix} 1 & 0.5774 & 0 \\ 0.5774 & 1.3333 & 0 \\ 0 & 0 & 1 \end{bmatrix}, \tag{3.32}$$

interpreted in the (x, y, z) space.

Following the design procedure presented in Section 3.3, we start with choosing the angle ϕ_2 for both media. If we set the second branches of the unit cells modeling the two media to be aligned in the $\hat{q}_2^a = \hat{q}_2^b = \hat{y}$ directions ($\phi_2^a = \phi_2^b = 90^\circ$), these two parameter values result in the directions of the first branches given by $\phi_1^a = -20^\circ$ and $\phi_2^b = 30^\circ$ via (3.20). Then, from (3.17)—(3.19), diagonal tensor elements for medium a are equal to

$$\mu_{11}^a = 1.0642, \quad \mu_{22}^a = 0.9397, \quad \epsilon_{33}^a = 0.9397 \tag{3.33}$$

in the (q_1^a, q_2^a, q_3^a) system. Similarly, diagonal tensor elements for medium b are found to be

$$\mu_{11}^b = 1.1547, \quad \mu_{22}^b = 0.8660, \quad \epsilon_{33}^b = 0.8660 \tag{3.34}$$

in the (q_1^b, q_2^b, q_3^b) system. Finally, the immittance values of the unit cells are computed via (3.21)—(3.23). The exact analytical solution for the $\hat{z}$-directed electric field E_z is known in terms of a simple transform of the field distribution for a line source radiating in free space.

Common to both media, the per-unit-length inductance and capacitance of the host TL grid were chosen to be $L_0' = 25.88\text{nH}/\lambda_0$ and $C_0' = 20.70\text{pF}/\lambda_0$ where λ_0 denotes the guided wavelength of the unloaded TL grid serving as a reference (free space). The intrinsic impedance of this TL grid is then equal to $Z_0 = \sqrt{L_0'/C_0'} = 35.36\ \Omega$. The unit

Table 3.1. Lumped element values for the host TL and the loading elements for both media.

Medium	Host		Loading					
	L_{01}, L_{02}	C_0	L_{Z1}	C_{Z1}	L_{Z2}	C_{Z2}	L_Y	C_Y
a	2.588 nH	2.070 pF	–	90.40 pF	0.1661 nH	–	113 nH	–
b			–	13.68 pF	0.4004 nH	–	50.86 nH	–

cell dimensions were uniformly chosen to be $p_1^a = p_2^a = p_3^a = p_1^b = p_2^b = p_3^b = p_0 = \lambda_0/10$. This choice of p_0 together with the values of L_0' and C_0' determined the operating frequency to be $f = 1.34$ GHz via the dispersion relation for the non-orthogonal grid network [26]. Both the host TL grid and reactive load elements were modeled using lossless lumped circuit components. Lumped component values for the series impedances and the shunt admittance in the two media are tabulated in Table 3.1 with terminating resistive load values equal to the Bloch impedance Z_B for a normally-incident plane wave [26].

Cells along the medium interface at $x = 0$, should be constructed with care. For a cell having the junction of the three paths positioned at the interface, let the series impedance in the $\hat{q}_2$ direction and the shunt admittance be denoted by Z_2^{ab} and Y^{ab}, respectively. Each should contain contributions from the media on both sides and they are connected in parallel. Therefore, their values are equal to $Z_2^{ab} = 2Z_2^a Z_2^b/(Z_2^a + Z_2^b)$, $Y^{ab} = (Y^a + Y^b)/2$. In essence, the procedure is superposing the properties of both media on both sides of the interface [28].

The circuit network was modeled and simulated using Agilent Advanced Design System (ADS) on a 60×40 grid of unit cells. A current source injecting 1 mA into the circuit network was positioned at $(x_0, y_0) = (-0.4698\lambda_0, 0.1710\lambda_0)$, which can be associated with a cell port in the ADS setup. At 1.34 GHz, the node voltage distribution was recorded. Then the node voltages were converted to $E_z = E_3$ via the relationship (3.6). As to the exact analytical solution, cylindrical fields are first obtained for a line source carrying a current of 1 mA in the $+\hat{z}$ direction located at $(-0.4698\lambda_0, 0)$ in a reference homogeneous medium

with an intrinsic impedance Z_0. Then, the solution is transformed according to (3.30) to arrive at the exact field distribution for the problem under consideration.

Figure 3.5 compares the field distributions from the TL metamaterial simulation and the analytical solution. Figures 3.5(a) and 3.5(b) plot the phase and magnitude responses from the circuit simulation, and Figures 3.5(c) and 3.5(d) show the analytical counterparts. It is noted that the field results are unnormalized values corresponding to a line source carrying a 1 mA current for both solution methods. The phase distributions in Figures 3.5(a) and 3.5(c) show an excellent agreement in both media a ($x < 0$) and b ($x > 0$). The field magnitude distribution in Figure 3.5(b) closely agrees with the analytical response in Figure 3.5(d) in the two media. Some irregularity appears in the simulation results, which is due to spurious reflections from the truncation boundary for obliquely incident wave components. However, their impact on the overall solution is minor. For a closer evaluation of the accuracy of the TL metamaterial solution, E_z along a horizontal line $y = 0.1710\lambda_0$ through the line source is plotted in Figure 3.6. Excellent agreements are obtained in both media between simulation and exact results for both real and imaginary parts of the electric field. An obvious exception is $\mathrm{Im}\{E_z\}$ at the source position, which diverges to ∞ for the analytical solution. As intended, note that no indication of reflection from the linear interface is observed. Numerical results in Figures 3.5 and 3.6 validate the non-orthogonal (parallelogram) unit cell design for 2D TL metamaterials for realizing full-tensor medium parameters. The key feature of the non-orthogonal grid is the simplicity of the unit cell construction while being capable of synthesizing any full-tensor anisotropic parameters.

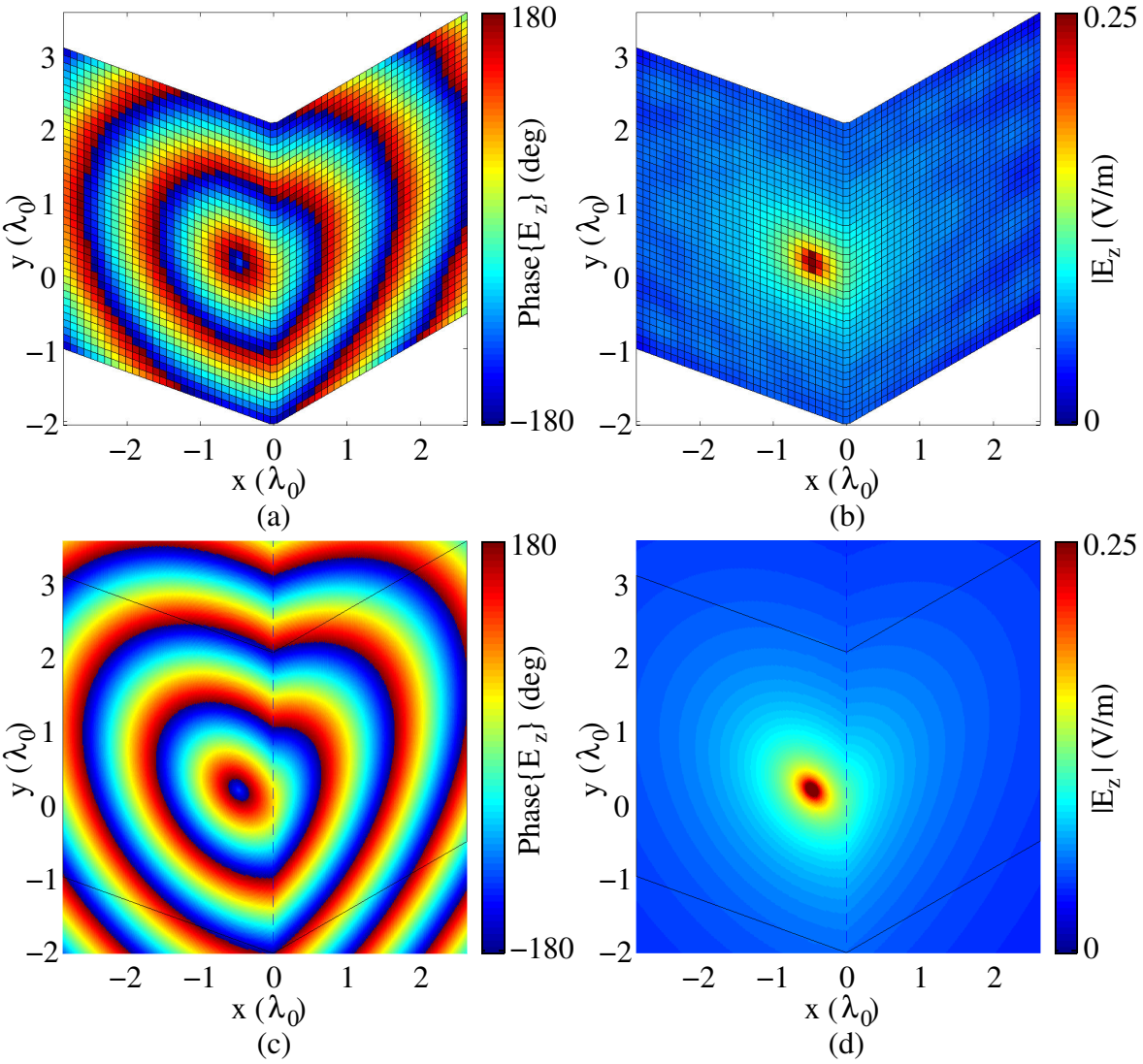

Figure 3.5. 2D distribution of the electric field E_z for a line source radiating near a linear interface. Numerical results for (a) Phase$\{E_z\}$ and (b) $|E_z|$. Exact analytical solutions for (c) Phase$\{E_z\}$ and (d) $|E_z|$. In (c) and (d), the boundary of the ADS simulation domain and the interface between the two media are indicated by black solid and dashed lines, respectively.

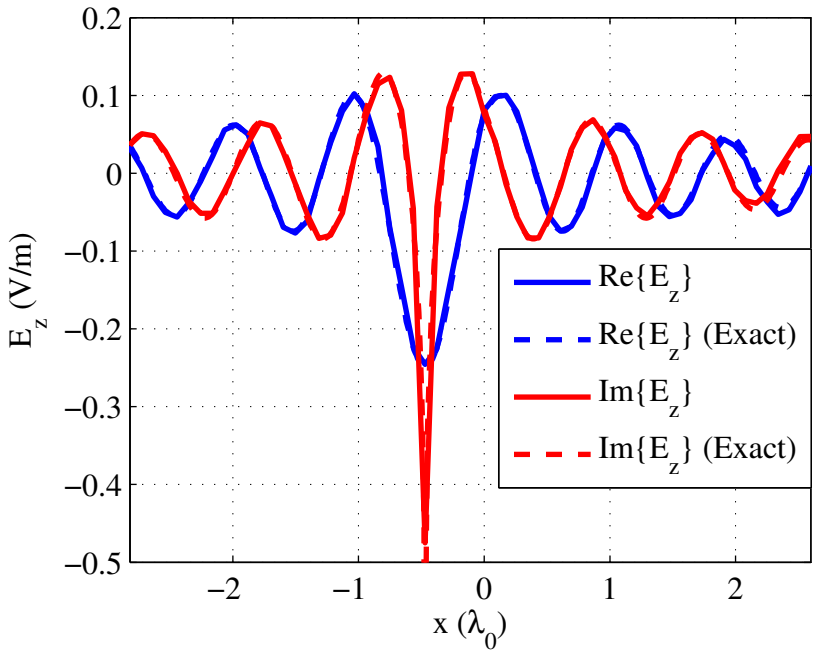

Figure 3.6. The electric field distribution along the horizontal line through the line source.

CHAPTER 4

TL METAMATERIAL CELL DESIGNS

In this chapter, unit cell designs for all regions in Figure 2.1(b) and, in addition, unit cells for region interfaces and boundaries are presented.

Rather than specifying a specific planar TL such as a stripline or microstrip, we represent short TL sections in a unit cell with equivalent lumped elements. This will keep the metamaterial designs in the following subsections general. Once the equivalent series inductance and shunt capacitance values are determined, the host TL can be implemented to meet the requirements. We use the shunt node configuration [27] to model the TE polarization of Figure 2.1.

4.1 Orthogonal-Grid (Rectangular) Unit Cell for A_1 and A_5

A conventional rectangular unit cell is shown in Figure 4.1(a), where lumped elements are physically aligned in the $\hat{q}_1 = \hat{x}$ and $\hat{q}_2 = \hat{y}$ directions. The values of shunt admittance Y and the series impedances Z_1, Z_2 in the two branches are given by

$$Y = Y_0 + Y_l, \quad Z_1 = Z_{10} + Z_{1l}, \quad Z_2 = Z_{20} + Z_{2l}, \tag{4.1}$$

where Y_0 and Z_{10}, Z_{20} are the immittances corresponding to the host TL section, i.e. the unloaded unit cell, and are equal to

$$Y_0 = j\omega C_0, \quad Z_{10} = j\omega L_{01}, \quad Z_{20} = j\omega L_{02}. \tag{4.2}$$

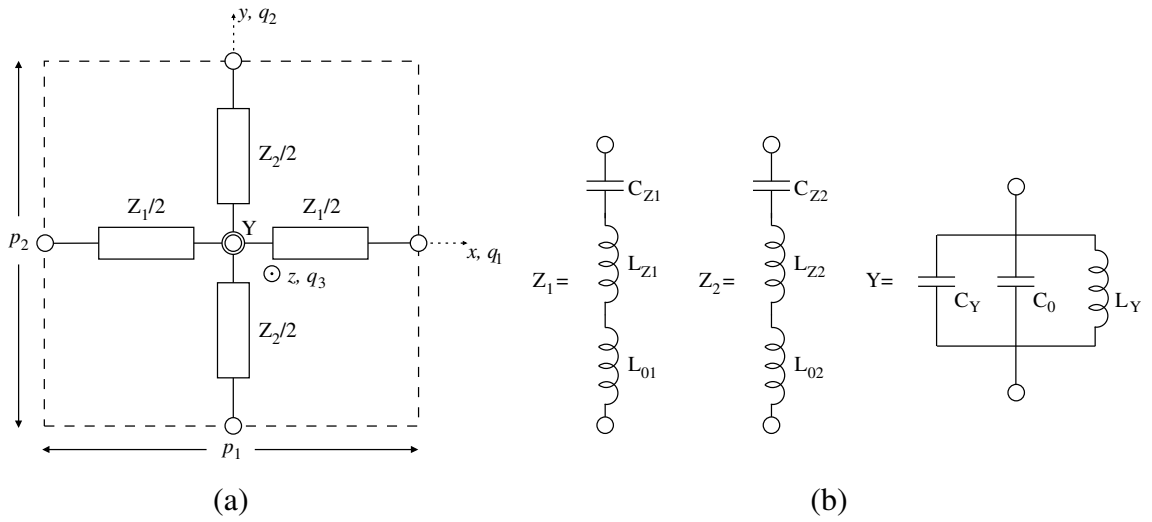

Figure 4.1. The TL unit cell and its immittances. (a) Top view of the orthogonal grid (rectangular) unit cell. (b) Definitions for Z_1, Z_2 and Y in terms of lumped components.

For unit cell dimensions p_1, p_2, p_3 in the $\hat{q}_1, \hat{q}_2, \hat{q}_3$ directions, from (3.24) we have

$$C_0 = \frac{p_1 p_2}{p_3} C_0', \quad L_{01} = \frac{p_1 p_3}{p_2} L_0', \quad L_{02} = \frac{p_2 p_3}{p_1} L_0', \tag{4.3}$$

where L_0' and C_0' are the per-unit-length series inductance and shunt capacitance, respectively, for the lumped model of a lossless TL with characteristic impedance of Z_0 and wavenumber $k_0 = 2\pi/\lambda_0$ (λ_0=guided wavelength of the host TL grid). Y_l and Z_{1l}, Z_{2l} in (4.1) are the shunt load admittance and series load impedances, respectively. Y, Z_1 and Z_2 are given in Figure 4.1(b) in their general form, composed of lumped components.

For realizing diagonal tensor parameters, such as those for A_1, A_4 and A_5, with arbitrary diagonal elements, given by

$$\boldsymbol{\mu} = \begin{bmatrix} \mu_{xx} & 0 \\ 0 & \mu_{yy} \end{bmatrix}, \epsilon_{zz}, \tag{4.4}$$

the values of Y, Z_1 and Z_2 are found to be [14]

$$Y = \epsilon_{zz} Y_0, \quad Z_1 = \mu_{yy} Z_{10}, \quad Z_2 = \mu_{xx} Z_{20}. \tag{4.5}$$

From (4.1) and (4.5), the values of reactive loading elements can be computed. For A_1 and A_5 representing unloaded TL grid regions, the load values are simply equal to zero. A_4 is a NIM lens region with $\mu_{xx} = \mu_{yy} = \epsilon_{zz} = -1$. Via (4.5) one can find the load values

$$Y_l = -2Y_0, \quad Z_{1l} = -2Z_{10}, \quad Z_{2l} = -2Z_{20}, \tag{4.6}$$

where Y_0, Z_{10} and Z_{20} are as given in (4.2).

Finally, dimensions $p_1 = p_2 = p_3 = p_0$ are chosen for the unit cells of A_1, A_4 and A_5 for some fixed length p_0.

4.2 Non-Orthogonal Grid (Parallelogram) Unit Cell for A_2 and A_3

Since A_2 and A_3 are anisotropic regions with non-zero off-diagonal tensor elements expressed in Cartesian system, the non-orthogonal grid unit cell presented in Chapter 3 is employed.

Define a non-orthogonal (q_1, q_2, q_3) coordinate system with the coordinate axes as indicated in Figure 4.2. Here, the q_1 axis makes an angle α from the $+\hat{x}$ direction in the $x - y$ plane. By properly choosing the shunt admittance load at the junction and the series impedance loads in the two branches, an effective medium with the following diagonal tensor parameters written in the (q_1, q_2, q_3) system can be synthesized:

$$\boldsymbol{\mu} = \begin{bmatrix} \mu_{11} & 0 \\ 0 & \mu_{22} \end{bmatrix}, \epsilon = \epsilon_{33}. \tag{4.7}$$

Similar to (4.5), the total shunt admittance Y and the series impedances Z_1, Z_2 are given in terms of μ_{11}, μ_{22} and ϵ_{33} as

$$Y = \epsilon_{33}Y_0, \quad Z_1 = \mu_{22}Z_{10}, \quad Z_2 = \mu_{11}Z_{20}. \tag{4.8}$$

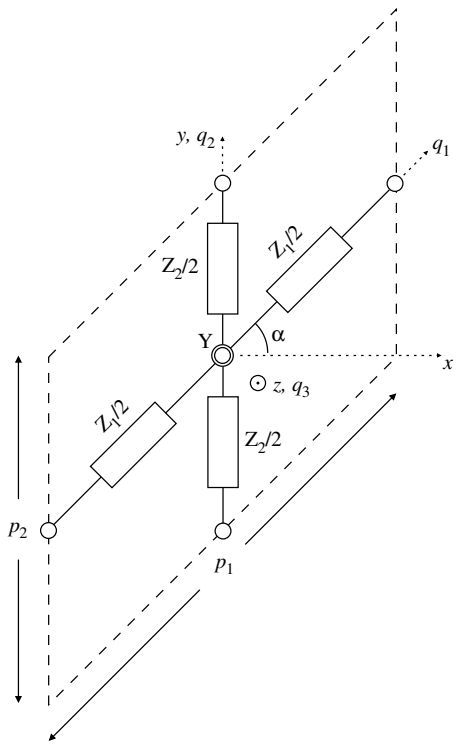

Figure 4.2. Top view of the non-orthogonal grid (paralleogram) unit cell.

Now, from Chapter 3, the material tensor values of (4.8) can be written in the (x, y, z) system as

$$\boldsymbol{\mu} = \begin{bmatrix} \mu_{11}\cos\alpha & \mu_{11}\sin\alpha \\ \mu_{11}\sin\alpha & \mu_{11}\frac{\sin^2\alpha}{cos\alpha} + \mu_{22}\frac{1}{\cos\alpha} \end{bmatrix}, \epsilon = \epsilon_{33}\frac{1}{\cos\alpha}. \tag{4.9}$$

Finally, four parameters μ_{11}, μ_{22}, ϵ_{33} and α can be properly determined to synthesize any full-tensor medium parameters written in the (x, y, z) system.

To realize the particular set of medium parameters for A_3 in (2.6), we obtain

$$\mu_{11} = \sqrt{2},\ \mu_{22} = 1/\sqrt{2},\ \epsilon_{33} = 1/\sqrt{2},\ \alpha = 45^\circ. \tag{4.10}$$

Although we are free to choose any set of values for p_1, p_2 as long as $k_0 p_1 \ll 1$, $k_0 p_2 \ll 1$ for each region, it is desirable to select the periods such that grids from two

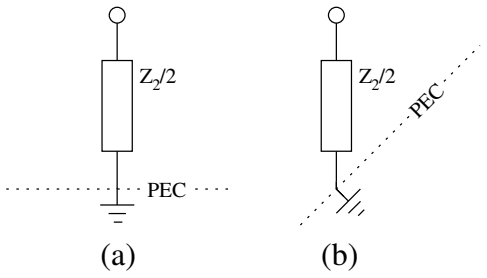

Figure 4.3. Boundary elements. (a) Half-cell element for the bottom of the recess and the surrounding flat ground plane. (b) Half-cell element for the slanted boundary of the recess.

adjoining regions to coincide for smooth transition across a common boundary. For the grids running in the $\hat{q}_2 = \hat{y}$ direction to integrate easily with those of A_4, we choose

$$p_1 = p_0/\cos\alpha = p_0\sqrt{2},\ p_2 = p_3 = p_0. \tag{4.11}$$

According to (4.2)–(4.3), note that the immittances of the unloaded TL in a unit cell for A_2, A_3 will be different from those for A_1, A_4, A_5.

4.3 Boundary Elements and Terminations

The simulation domain of the TL metamaterial design is bounded by the ground recess and the surrounding ground plane from below. The open boundary on the remaining three sides is truncated with resistive terminations. For the conducting boundary, there are two different surfaces — flat and slanted — as shown in Figure 2.1(b). For the flat portion of the ground, half cells are used along the conducting boundary, i.e. the junction at the center of a unit cell is grounded. Along the flat boundary at the bottom of the recess and outside the recess, the short circuit shown in Figure 4.3(a) is used. The setup in Figure 4.3(b) is used along the slanted side walls of the recess. At each port along the truncation boundary of A_5, a terminating resistor with resistance equal to the Bloch impedance for a normally-incident plane wave [26, 29] is connected.

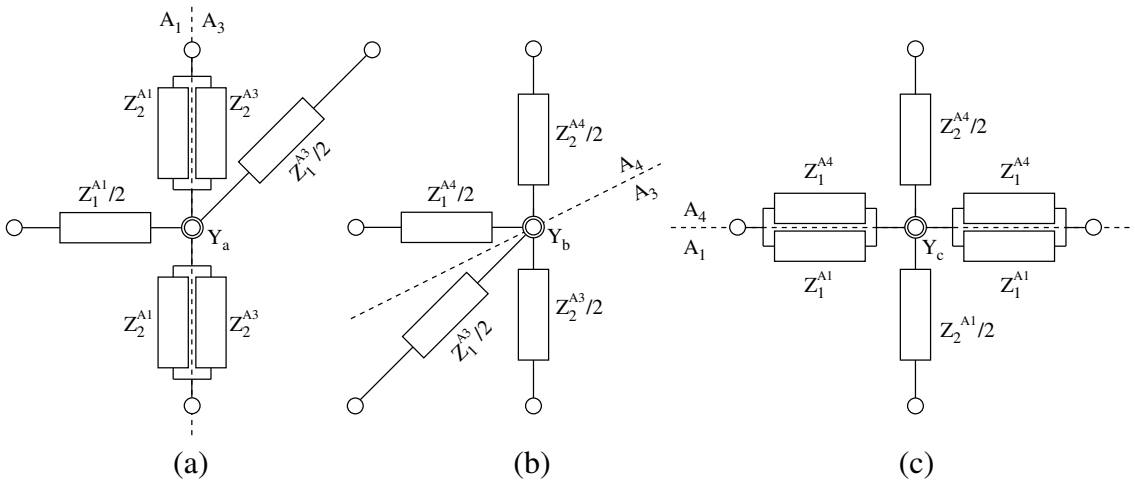

Figure 4.4. Definitions for the interface elements. (a) $A_1 - A_3$ interface. (c) $A_3 - A_4$ interface. (c) $A_1 - A_4$ interface element. In each case, a dashed line indicates the physical interface between two regions.

4.4 Interface Elements

For ease of physical realization, the coordinate transformation has been deliberately chosen to give homogeneous medium parameters for each region. Hence, medium parameters are discontinuous across every interface between two media. Any unit cell positioned along a medium boundary needs to be carefully designed. Since a unit cell is a discrete model of the area covered by the cell itself, the immittance values for a unit cell should incorporate medium parameters of every region it sits on. It should be stressed that choosing a full set of immittances associated with either one medium for an interface cell needs to be avoided; it amounts to shifting the position of the interface by half a unit cell dimension.

We construct boundary elements for each interface by superposing the properties of both sides of the interface [28]. Referring to Figure 4.1(a), the shunt admittance Y accounts for the total admittance for the whole unit cell, i.e. the sum of shunt admittances from the four quadrants. The series impedance $Z_1/2$ on the $+\hat{x}$ axis is responsible for the total impedance in the $\hat{x}$ direction in quadrants 1 and 4. The two impedances are shunt connected to form $Z_1/2$. Similarly, the impedance $Z_2/2$ is given by two impedances in the $\hat{y}$ direction in quadrants 1 and 2 in a shunt connection. Therefore, if a TL grid is chosen such that the

junction of the two branches is positioned along an interface, immittance values associated with individual quadrants can be properly selected to find the four series impedances and one shunt admittance.

Three interface elements should be defined for the embedded configuration along the $A_1 - A_3$, $A_3 - A_4$, and $A_1 - A_4$ interfaces. They are illustrated in Figure 5(a), (b) and (c), respectively. The shunt admittances are given by

$$Y_a = \frac{Y^{A_1}}{2} + \frac{Y^{A_3}}{2}, \quad Y_b = \frac{Y^{A_3}}{2} + \frac{Y^{A_4}}{2}, \quad Y_c = \frac{Y^{A_1}}{2} + \frac{Y^{A_4}}{2}. \tag{4.12}$$

In (4.12), the immittances Y_{A_k} and Z_{A_k} respectively, correspond to region A_k with k being the region number. Their values were found in Sections 4.1 and 4.2. Mirror images of the interface elements depicted in Figure 4.4(a) and 4.4(b) are used for the elements along the $A_1 - A_2$ and $A_2 - A_4$ interfaces, respectively.

CHAPTER 5

NUMERICAL RESULTS

5.1 Embedded Line Source in a Ground Recess

A numerical 2D circuit analysis was performed to validate the TL metamaterial design of the embedded line source radiation. Advanced Design System (ADS) from Agilent was used to simulate the 2D lumped-element network. For the host TL, $L_0' = 25.88$ nH$/\lambda_0$ and $C_0' = 20.70$ pF$/\lambda_0$ were selected to realize the characteristic impedance $Z_0 = 35.36\ \Omega$. Using the dispersion relation for the 2D composite right/left-handed network [14], the frequency of operation $f_0 = \omega_0/2\pi$ is calculated via

$$\omega_0 = \omega_R\sqrt{2(1-\cos k_0 p_0)}, \tag{5.1}$$

where $k_0 p_0$ is the per-unit-cell phase delay and $\omega_R = 1/\sqrt{L_{01}C_0}$. Setting $p_0 = \lambda_0/10$ ($k_0 p_0 = 0.2\pi$), design frequency is selected to be $f_0 = 1.34$ GHz. Finally, dimensional parameters of the ground recess were chosen to be $a = d = c/2 = 2h = 2t = \lambda_0$.

For the original and embedded radiation configurations in Figures 2.1(a)–(b), 2D circuit models for an area of $6\lambda_0 \times 4\lambda_0$ were created in ADS using 60 by 40 grid points. Complete structure of the embedding media is shown in Figure 5.1. The solid gray line shows the ground recess. Green and blue unit cells correspond to regions A_3 and A_4, respectively. Free space regions are shown with thinner black unit cells. Interface unit cells in Figures 4.4(a), 4.4(b), and 4.4(c) are shown in red, cyan, and magenta, respectively. A more detailed view over the area of the slanted recess wall is provided in Figure 5.2 to clearly show the non-orthogonal grid for A_3 and the three types of interface elements in place.

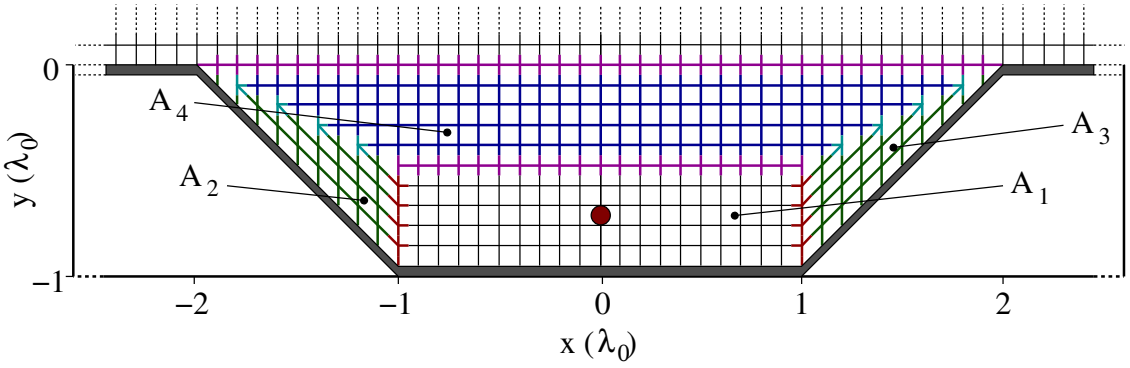

Figure 5.1. A detailed view of the TL metamaterial grid over the area of the embedding region.

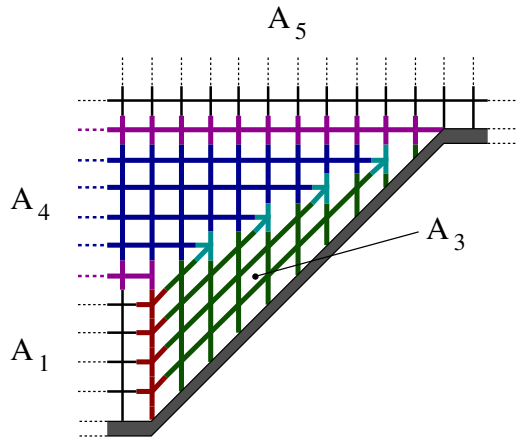

Figure 5.2. A detailed view of the TL metamaterial grid over the area of the slanted recess wall.

The lumped circuit element values for the host TL and the loading elements were computed from the expressions derived in Chapter 4 and they are tabulated in Table 5.1. The line source was modeled using an ideal AC current source at 1.34 GHz placed $\lambda_0/4$ above the ground plane at $(x, y) = (0, s = 0.25\lambda_0)$ for the original and at $(0, -0.75\lambda_0)$ for the embedded configurations. Voltages at the end of the vertical branches of each unit cell were recorded.

At the design frequency $f = 1.34$ GHz, Figure 5.3 shows a snapshot and the phase distribution of the node voltages at the current source phase of zero for the original config-

Table 5.1. Lumped element values for the host TL and the loading elements for each region.

	Host			Loading					
	L_{R1}	L_{R2}	C_R	L_{Z1}	C_{Z1}	L_{Z2}	C_{Z2}	L_Y	C_Y
A_1	2.588 nH	2.588 nH	2.070 pF	N/A					
A_2 A_3	3.660 nH	1.830 nH	2.927 pF	–	13.160 pF	0.758 nH	–	16.453 nH	–
A_4	2.588 nH	2.588 nH	2.070 pF	–	2.725 pF	–	2.725 pF	3.407 nH	–
A_5	2.588 nH	2.588 nH	2.070 pF	N/A					

uration of Figure 2.1(a). The results show excellent agreements with the available analytical solutions.

The same set of plots for the embedded configuration are shown in Figure 5.4 for comparison. In $y \geq 0$, Figures 5.3(a) and 5.4(a) show an excellent agreement that cannot be visually distinguished. A comparison of the phase distributions in Figures 5.3(b) and 5.4(b) clearly shows that the waves generated by the embedded configuration appear as if they originate above the ground plane as intended.

In contrast, the node voltage distribution for a source radiating inside a ground recess without any embedding media is shown in Figure 5.5. This distribution agrees with the 2D numerical analysis result based on effective medium parameters. It is observed that the radiation characteristics of the line source are significantly affected by the unfilled recess.

To quantify the fidelity of the proposed embedded design in reproducing the radiation characteristics of the original configuration, 2D far-field directivity patterns are computed and compared. Using a near-field to far-field transformation using the node voltages and branch currents from ADS along the truncation boundary of the simulation domain, a directivity pattern can be obtained. Detailed discussion for the numerical calculation is provided in Appendix A. In addition, one can obtain the exact far-field pattern for the original configuration at the design frequency analytically. It is equal to

$$D_{\text{exact}}(\phi) = \frac{\sin^2(\frac{\pi}{2}\sin\phi)}{2\pi\int_0^{\pi}\sin^2(\frac{\pi}{2}\sin\phi)d\phi}. \tag{5.2}$$

The 2D directivity patterns are compared in Figure 5.6 for the three configurations shown in Figures 5.3–5.5 together with the analytical result of the original configuration given in (5.2). The pattern curves for the original and embedded configurations lie on top of each other in the entire angular range of ϕ in $0 \leq \phi \leq \pi$ measured from the $+\hat{x}$ axis. This validates the effectiveness of the embedded configuration in reproducing the original radiation pattern at the design frequency, especially the non-orthogonal unit cell design in Figure 4.2 as well as the three interface elements in Figure 4.4. The very slight discrepancy between the analytical solution and the original/embedded configuration is attributed to discrete nature of the metamaterial design and a small amount of reflections from the open boundary of region A_5 for obliquely incident wave components. In contrast, the directivity pattern for the line source in an open recess exhibits a significant distortion.

The effect of loss on the performance is investigated by incorporating component losses to lumped load elements in A_2, A_3, and A_4. The host TL grids in A_1 and A_5 are treated lossless. In Figure 5.7, directivity patterns with different quality factor (Q) values of 100, 50, and 20 are compared with the lossless case. Although the radiation pattern deviates from that of the lossless case as Q is decreased, there is no significant degradation. Low-loss inductors and capacitors in the GHz range with the Q values up to 100 are commonly available, so it is anticipated that a TL metamaterial fabrication of the embedded design will exhibit a radiation pattern comparable to what is expected of a lossless design.

In addition to the performance at the design frequency, bandwidth characteristics of the metamaterial design are of great interest. Figure 5.8 shows 2D directivity patterns at $-2\%, -4\%, +2\%, +4\%$ away from $f = f_0$ as well as the design frequency. It is observed that the pattern degradation is more sensitive to a frequency increase than a decrease. The pattern bandwidth is further characterized by the relative rms error e_D defined by

$$e_D = \frac{\int_0^\pi |D(\phi) - D_{\text{exact}}|^2 d\phi}{\int_0^\pi |D_{\text{exact}}|^2 d\phi} \tag{5.3}$$

as a function of frequency. In (5.3), $D(\phi)$ is the directivity of the embedded configuration which changes with frequency and D_{exact} is the analytical directivity pattern of the original configuration fixed at $f = f_0$. The error e_D is plotted in Figure 5.9 at different frequencies. Using $e_D = 0.1$ as the reference, the pattern bandwidth is found to be approximately 8%.

The input impedance observed by the current probe was computed for the original and embedded configurations to assess the impedance bandwidth characteristics. A small amount of loss with $Q = 1000$ was added to the lumped load elements for the embedded case to help the ADS solution stabilize. In the absence of loss, there is no unique solution due to the presence of surface-mode plasmon resonances along the NIM boundaries. The input impedances $Z_{\text{in}} = R_{\text{in}} + jX_{\text{in}}$ are plotted with respect to frequency in Figure 5.10(a) for the two configurations. They turn out to be inductive and the reactances match each other at $f = f_0$. The slightly higher resistance for the embedded source is attributed to the added loss. The input impedance exhibits multiple resonances similar to the 3D monopole case predicted with effective medium parameter simulations [13]. Figure 5.10(b) shows the magnitude of the input reflection coefficient with a reference impedance of 10 Ω after a series capacitor was inserted at the driving port to cancel the inductive reactance. The impedance bandwidth of the embedded system is narrow compared with the original system, mainly due to the dispersion of the NIM in A_4.

Now we consider the same embedded line source radiation case with increasing the resolution of the discrete unit cell TL metamaterial design. Keeping the same parameters for the host TL, $L_0' = 25.88$ nH$/\lambda_0$ and $C_0' = 20.70$ pF$/\lambda_0$ to realize the characteristic impedance $Z_0 = 35.36\,\Omega$, we chose $p_0 = \lambda_0/20$ which doubled the resolution of the circuit model. The new design frequency was determined to be $f_0 = 0.68$ GHz according to the dispersion relation given in 5.1. The dimensional parameters of the ground recess were chosen to be $a = d = c/2 = 2h = 2t = \lambda_0/2$. At the design frequency, the lumped

circuit element values for the host TL and the loading elements were computed similar to the previous design. The line source was modeled using an ideal AC current source at 0.68 GHz placed $\lambda_0/8$ above the ground plane at $(x, y) = (0, s = 0.125\lambda_0)$ for the original and at $(0, -0.375\lambda_0)$ for the embedded configurations. With doubled resolution, the same 2D circuit model of 60 by 40 grid points now represents a simulation area of $3\lambda_0 \times 2\lambda_0$.

At the new design frequency $f = 0.68$ GHz, Figure 5.11 shows a snapshot of the node voltages at the current source phase of zero for both original and embedded configurations. The agreement between the node voltage distributions of Figure 5.11 was further investigated via 2D directivity patterns. Figure 5.12 shows directivity patterns for the two configurations shown in Figures 5.11(a) and (b) together with the analytical result of the original configuration. We observed that the pattern curves for the original and embedded configurations lie on top of each other and follow the exact pattern of the analytical result of the original configuration.

5.2 Embedded Line Source Array in a Ground Recess

In this subsection, we consider an embedded array configuration inside a ground recess, where a horizontal array is embedded inside the designed embedding media.

Consider a 2D horizontal array of N line sources carrying complex currents I_n $(n = 1, 2, ..., N)$ positioned at $(\mathbf{r_n}, y_0)$, where $\mathbf{r_n} = \hat{x}[n-(N+1)/2)]d$ and d is the interelement spacing. A seven-element linear array is illustrated in Figure 5.13. To demonstrate a pattern null in the broadside direction $\hat{y}$, and a pattern maximum close to the end-fire direction, we chose I_n to be

$$I_n = e^{j\frac{4\pi}{7d}\hat{x}\cdot\mathbf{r_n}}. \tag{5.4}$$

The seven-element line source array with $d = 0.3\lambda_0$ was simulated inside the ground recess at $y_0 = -0.75\lambda_0$ and the same array was also simulated above the ground plane positioned at $y_0 = 0.25\lambda_0$. Snapshots of the node voltage distribution are shown in Figure 5.14 for

the two configurations. As expected, in $y \geq 0$, Figures 5.14(a) and 5.14(b) are in excellent agreement that cannot be visually distinguished.

In Chapter 2, A_2 and A_3 were interpreted as impedance-matching regions, compensating the truncation effect associated with the finite horizontal dimension of the NIM lens. Now, we consider the case where high loss values are introduced for A_2 and A_3. This case was examined by incorporating component losses to both lumped load elements and to lumped elements corresponding to host TL grids in A_2 and A_3. This is, in effect cancelling the waveguiding function of the impedance-matching regions. The same seven-element array of Figure 5.13 was embedded inside the ground recess. For the loss tangent value, $\tan\delta = 1$, Figure 5.15 shows a snapshot of the node voltage distribution. In comparison to Figure 5.14(a), the distortion in the pattern is visually distinguishable. In Figure 5.16, directivity patterns with different $\tan\delta$ values of 1 and 5 are compared with the lossless case. We observed that, functionally removing A_2 and A_3 distorts the far field pattern. This example emphasizes the importance of the impedance-matching regions.

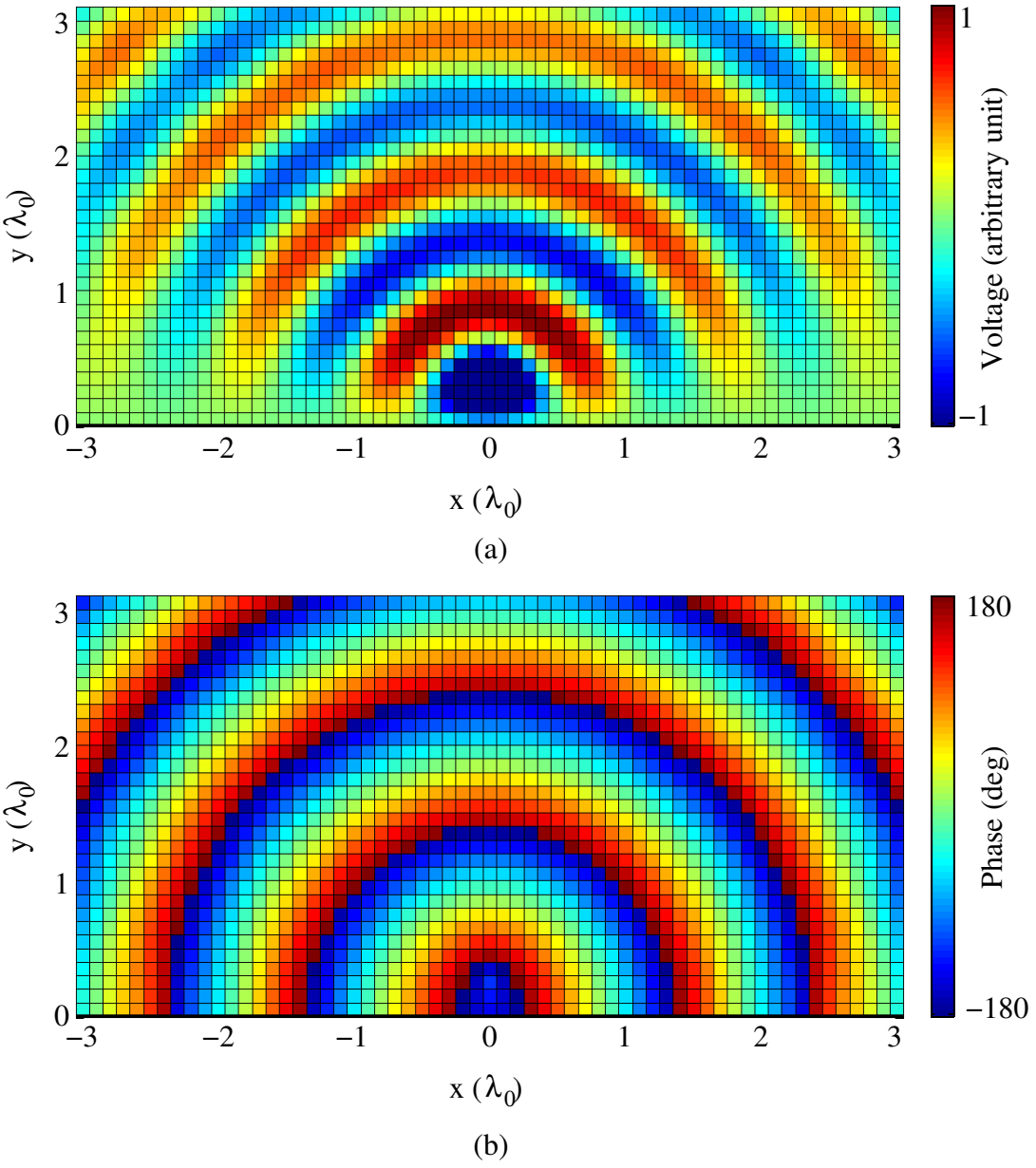

Figure 5.3. Node voltage distribution for the original configuration. (a) A snapshot. (b) Phase distribution. Both are referenced to the current source phase zero.

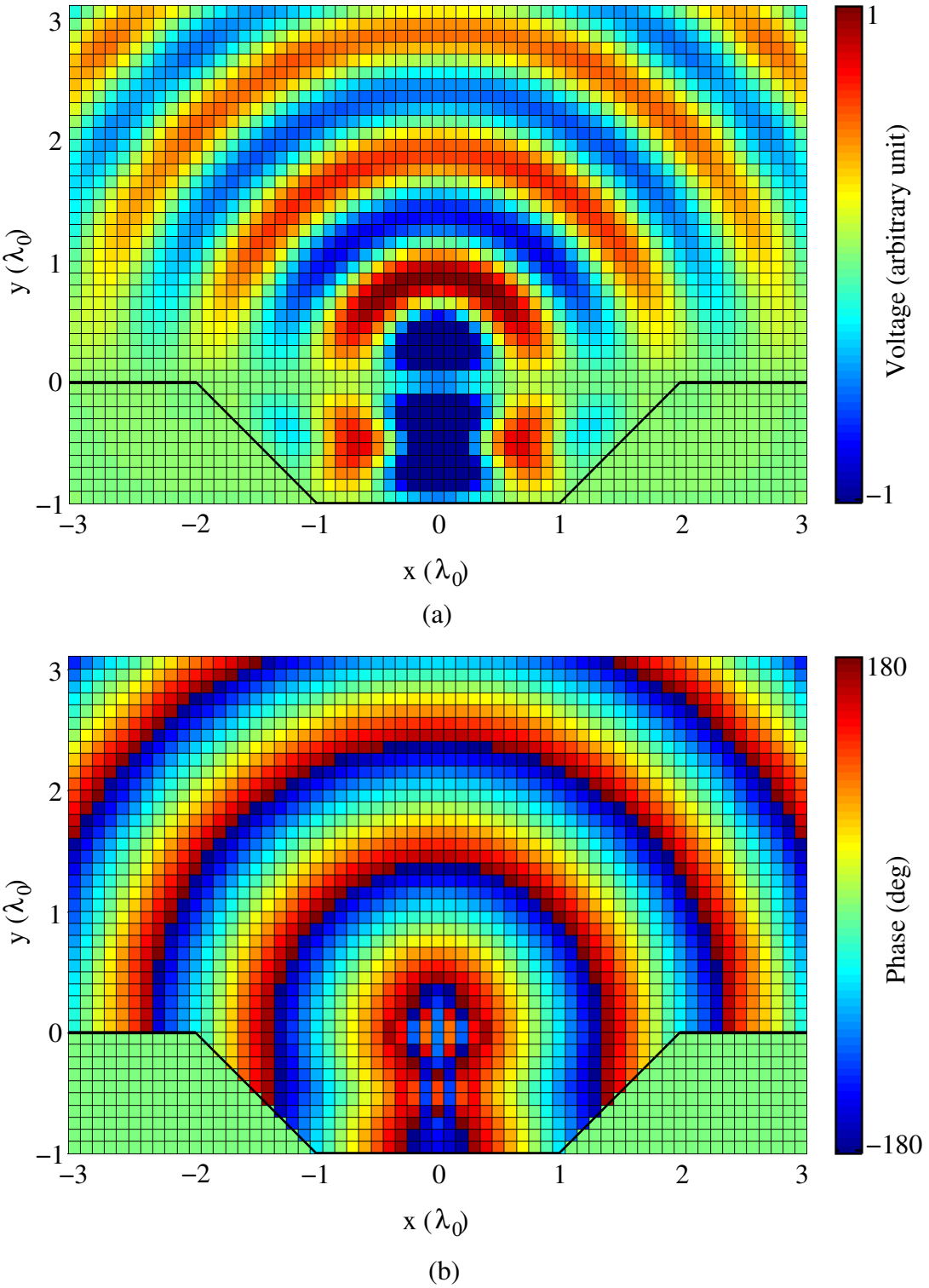

Figure 5.4. Node voltage distribution for the embedded configuration. (a) A snapshot. (b) Phase distribution.

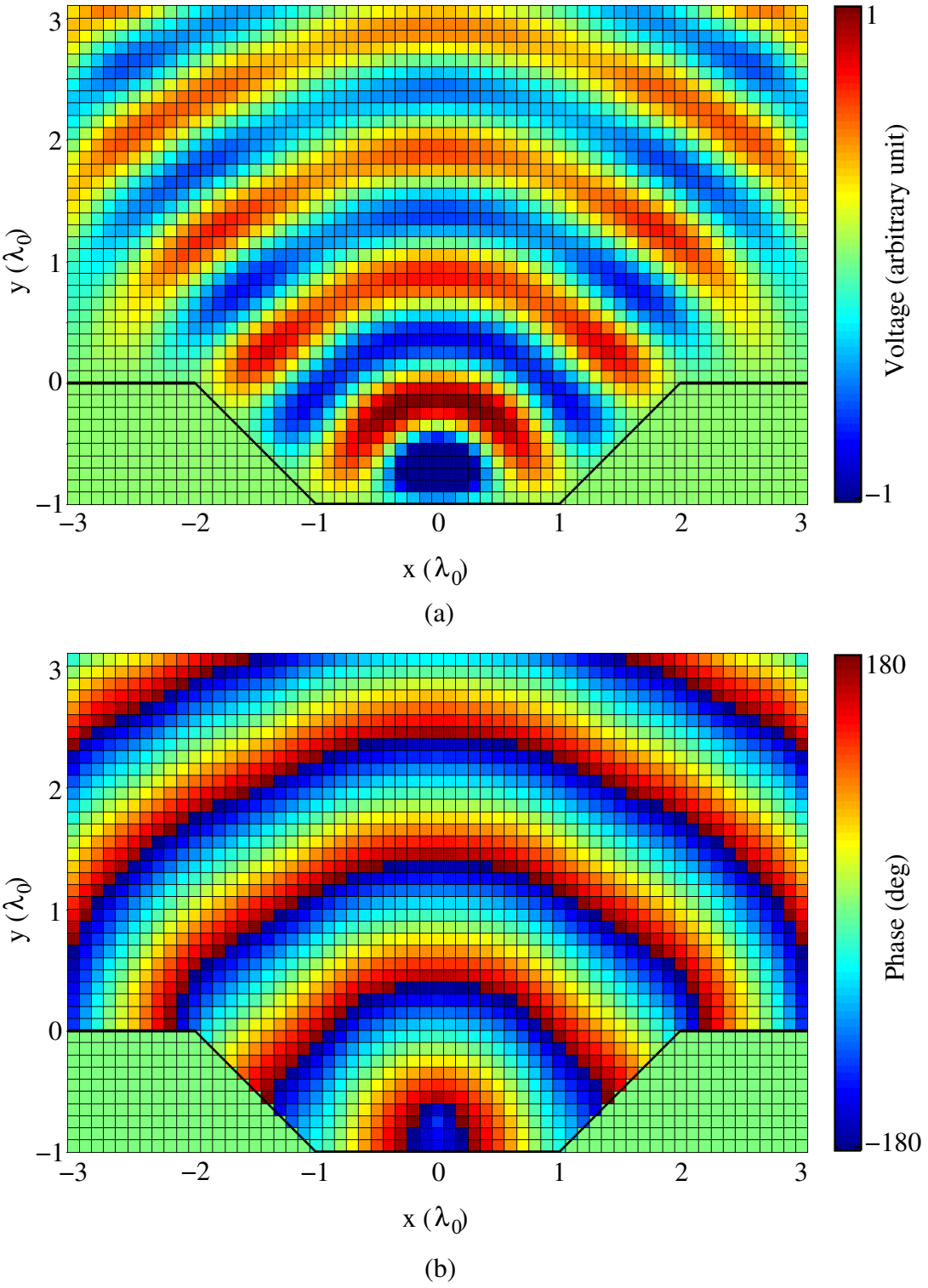

Figure 5.5. A snapshot of the node voltage distribution for a source inside the ground recess without any embedding media.

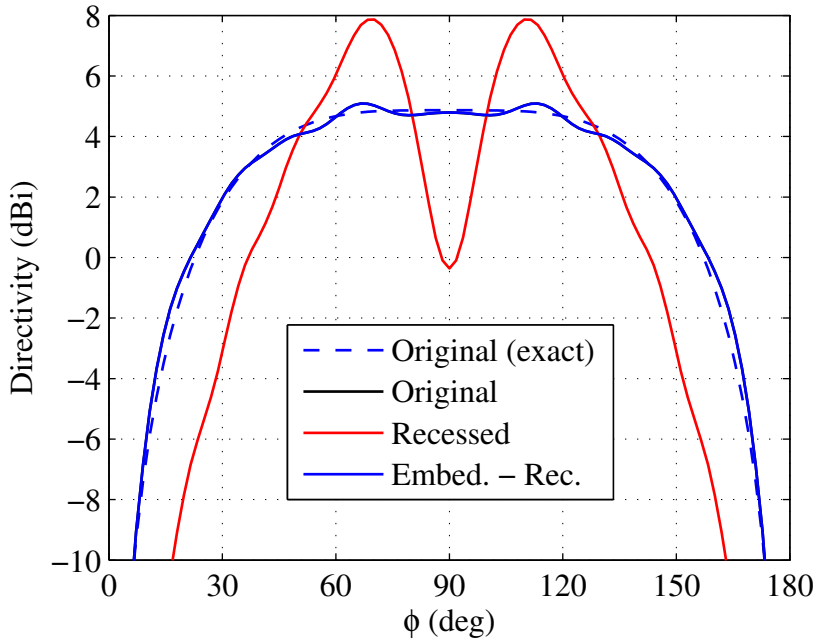

Figure 5.6. 2D directivity patterns for the original, recessed and embedded configurations compared with the analytical solution for the pattern of the original configuration.

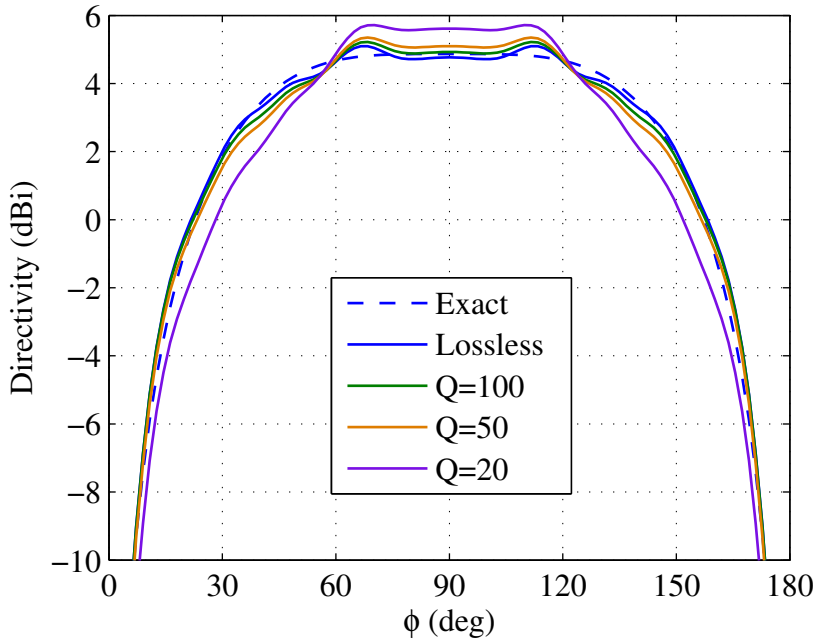

Figure 5.7. Effect of loss in terms of Q for the load elements on the radiation pattern. Directivity patterns for $Q = 100$, 50, 20, and the lossless cases are compared with the analytical directivity pattern of the original configuration.

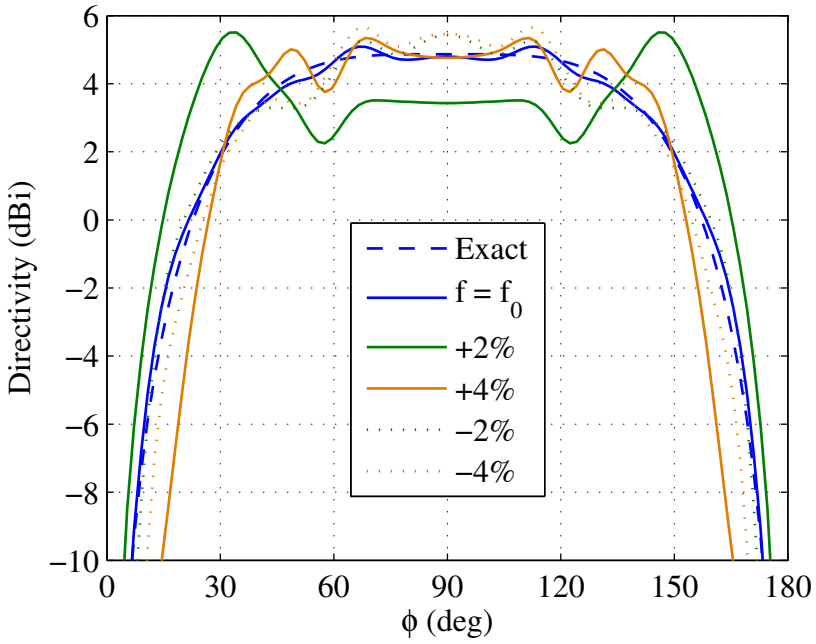

Figure 5.8. Directivity patterns for the embedded system at different frequencies.

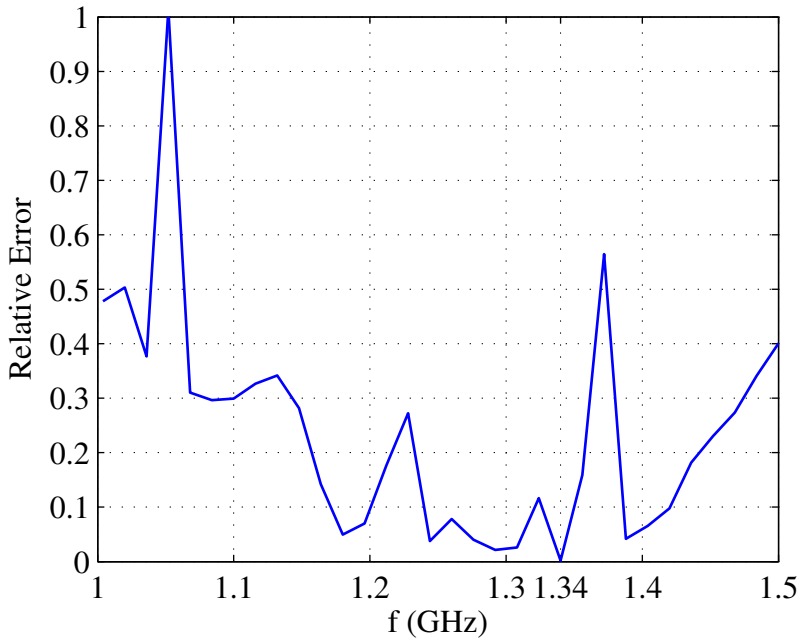

Figure 5.9. Relative error of the far-field pattern at different frequencies.

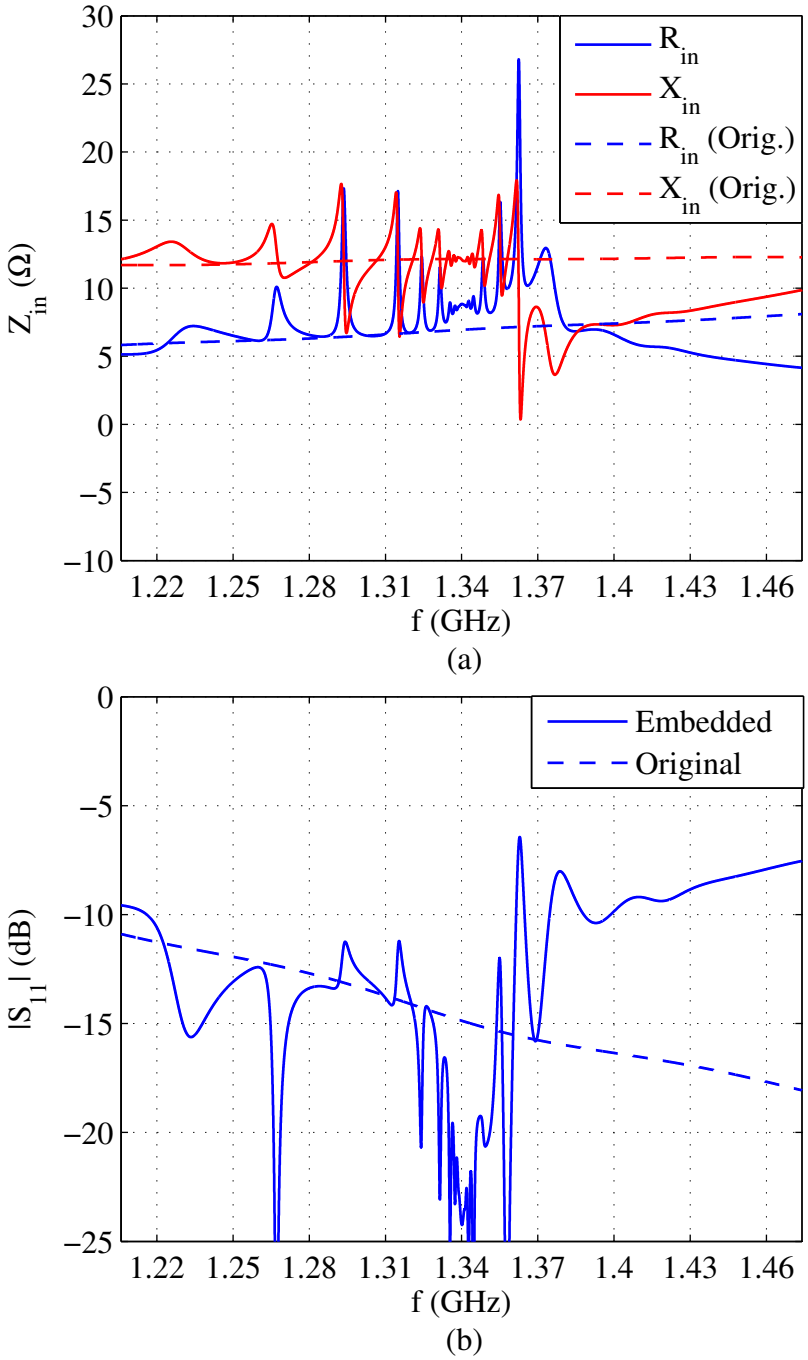

Figure 5.10. The impedance bandwidth characteristics of the embedded configuration compared with the original. (a) The input impedance. (b) The input reflection coefficient with respect to frequency, relative to 10 Ω. A series capacitor of 9.78 pF has been used to eliminate the inductive reactance.

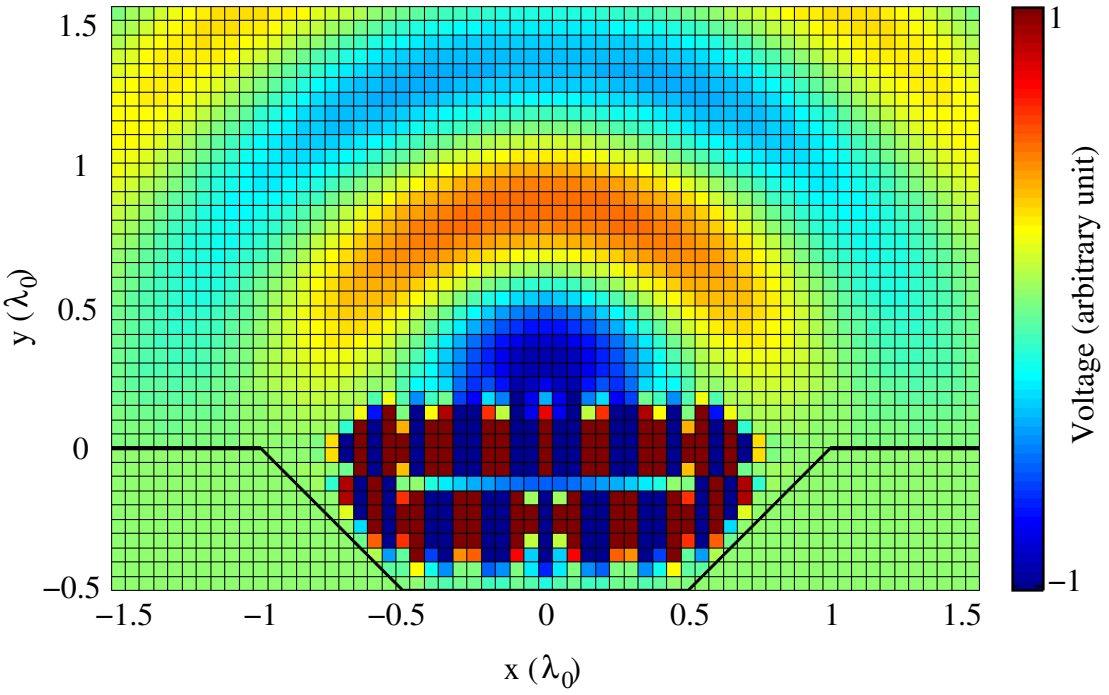

(a)

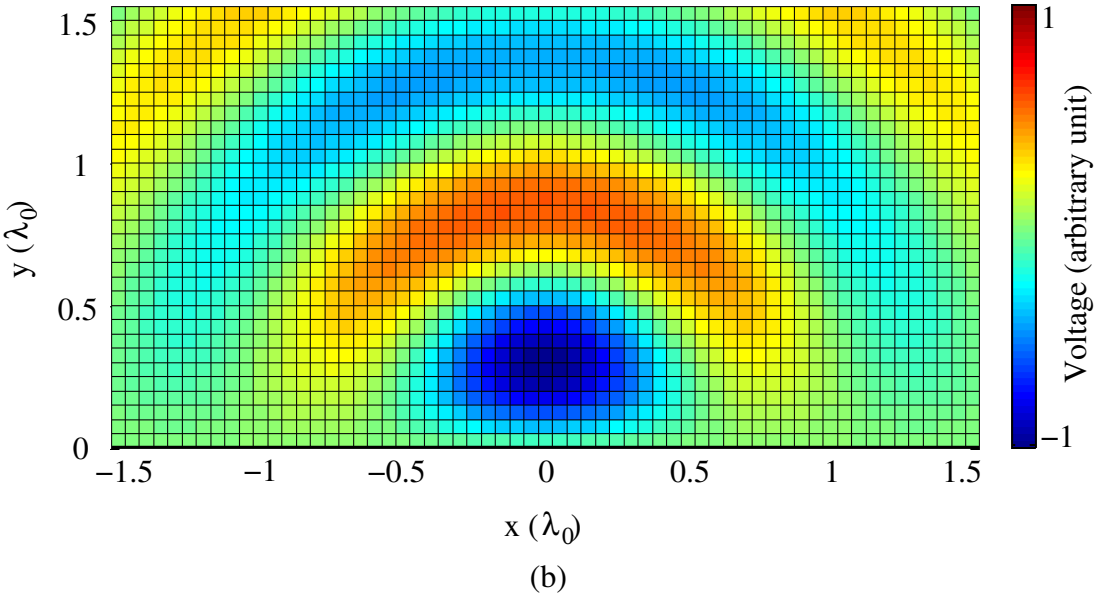

(b)

Figure 5.11. Effect of increased resolution on the radiation pattern for $p_0 = \lambda_0/20$. Snapshots of the node voltage distributions. (a) Embedded configuration. (b) Original configuration.

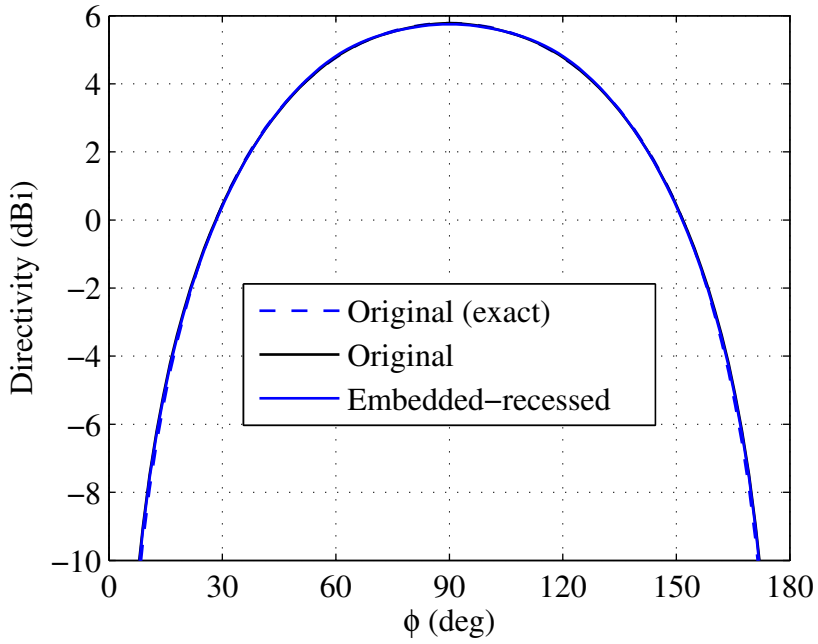

Figure 5.12. Effect of increased resolution on the radiation pattern for $p_0 = \lambda_0/20$. 2D directivity patterns for the original and embedded configurations compared with the analytical solution for the pattern of the original configuration.

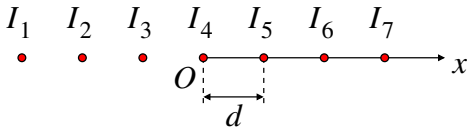

Figure 5.13. A 2D horizontal array of $N = 7$ line sources.

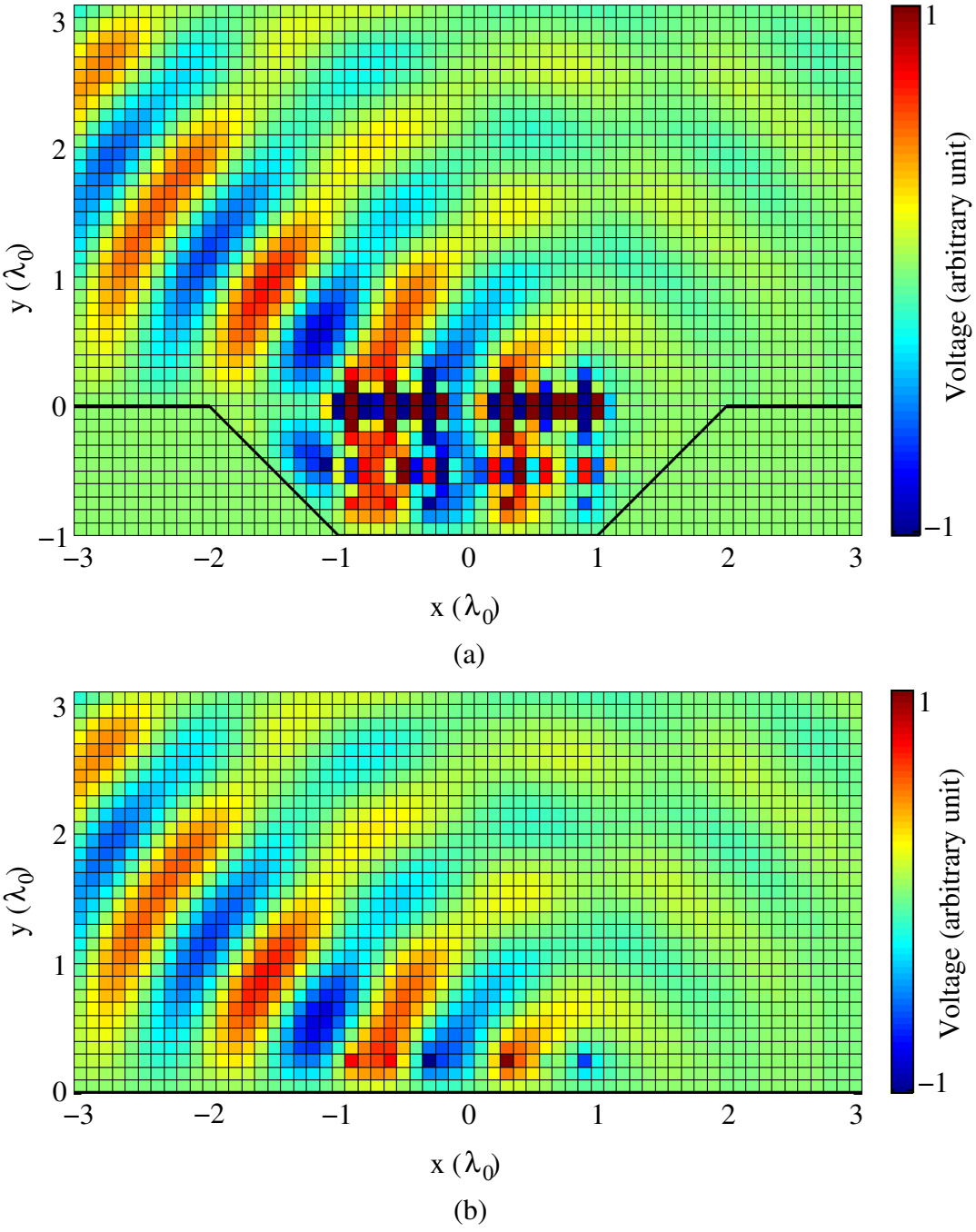

Figure 5.14. Snapshots of the node voltage distributions for array configurations. (a) Embedded-array inside a ground recess. (b) Array above the ground plane.

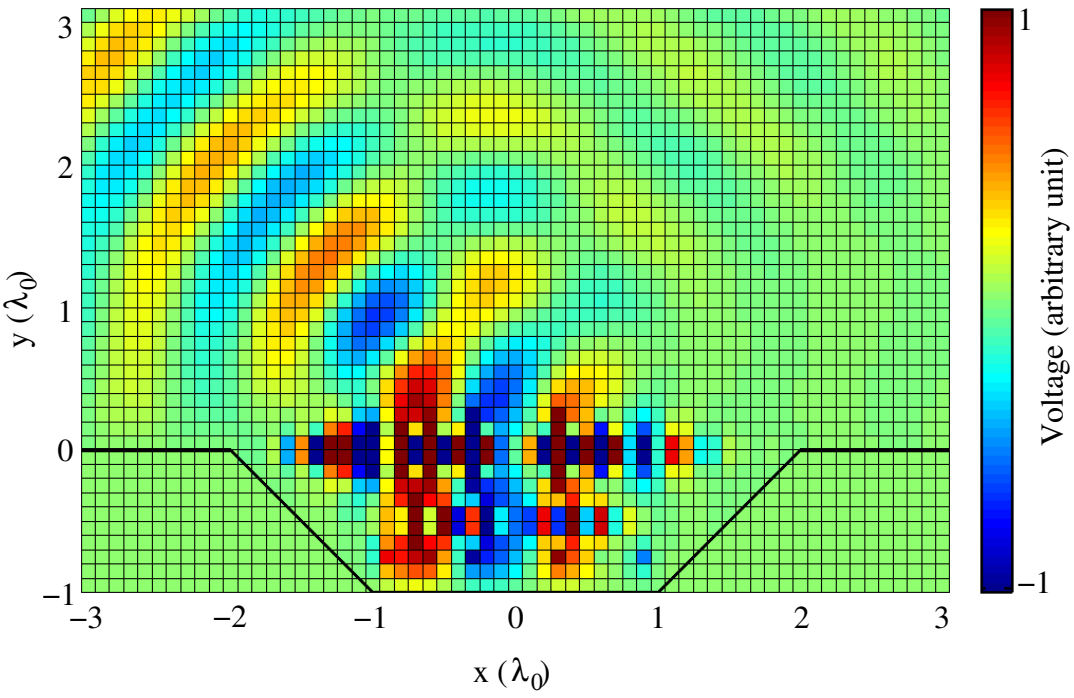

Figure 5.15. Effect of lossy A_2 and A_3 for $\tan\delta = 1$. A snapshot of the node voltage distribution.

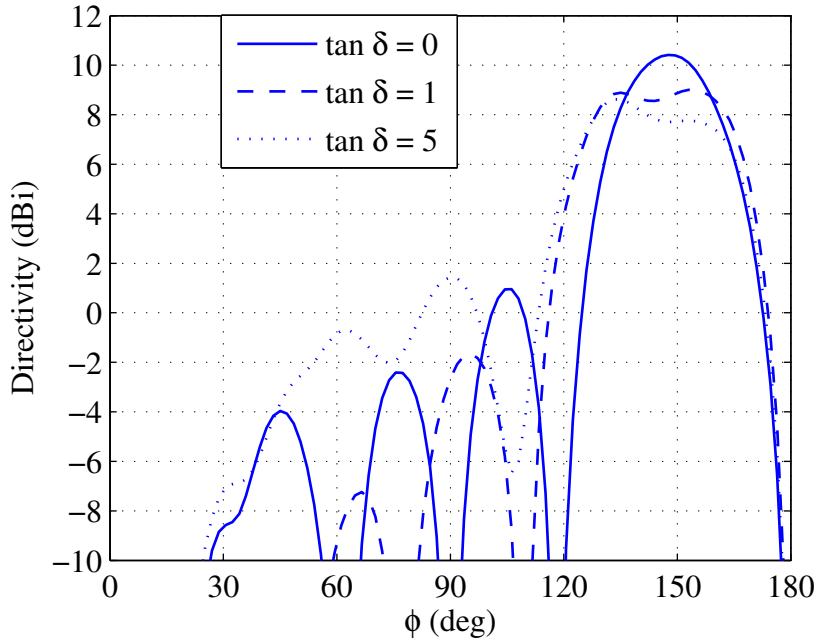

Figure 5.16. Effect of lossy A_2 and A_3 for different loss tangent values. Directivity patterns for $\tan\delta = 1$ and $\tan\delta = 5$ are compared with the lossless case.

CHAPTER 6

CONCLUSIONS

A 2D TL metamaterial design of an embedded line source radiation based on the coordinate transformation approach has been presented. The line source inside a ground recess is embedded in metamaterials such that it creates the same waves away from the source as a line source in free space above the ground plane. TL metamaterial unit cell designs for the NIM lens region and the anisotropic impedance-matching regions were presented. The impedance-matching regions were realized with a novel non-orthogonal grid unit cell. The performance of this cell was examined via a line source radiation configuration near a reflectionless interface. The final embedding media were numerically analyzed via circuit simulations. Numerical results show an accurate reproduction of the radiation characteristics by the embedded design at the design frequency. The effect of loss is predicted to be minimal with low-loss reactive loading elements. Predicted pattern and impedance bandwidth characteristics have been presented.

The proposed metamaterial design may be realized by loading a host TL such as a 2D microstrip network with lumped reactive loading elements. The ground plane and the recess can be realized using a series of vias along the conducting boundary. Resistors can terminate the truncation boundary of the 2D TL network.

Due to the simplicity of the unit cell structure representing the anisotropic impedance-matching regions, the TL metamaterial design can be extended to a resonator-based metamaterial counterpart in a straightforward manner. For the anisotropic regions in the 2D metamaterial, a unit cell in the form of a cylindrical shell with a parallelogram cross section can be used. Electric and magnetic resonators positioned on the tilted side walls will

be able to synthesize any anisotropic tensor medium parameters expressed in the Cartesian coordinate system.

APPENDIX

CALCULATION OF 2D FAR-FIELD RADIATION PATTERNS

Near-field to far-field transformation method is utilized to extract the far-field radiation pattern from the boundary voltages and branch currents of the associated TL grid structure. A circuit network boundary is illustrated in Figure A.1 with a PEC ground plane at $y = 0$. Node locations are indicated with red dots and the associated branches are marked with arrows. The isomorphism relations between the node voltages, branch currents and the fields for the TE polarization were derived in Chapter 3 as given in (3.6). Accordingly, the surface electric field and the surface magnetic field intensities $\mathbf{E_s}$ and $\mathbf{H_s}$, respectively, are equal to

$$\mathbf{E_s} = -\hat{z}\frac{V}{p_0}, \quad \mathbf{H_s} = \hat{c}\frac{I}{p_0} \tag{A.1}$$

in the Cartesian (x, y, z) coordinate system, where p_0 is the fixed unit cell dimension of the orthogonal unit cell for region A_5. The c direction is indicated for each part of the piecewise continuous boundary in Figure A.1. The surface electric current density $\mathbf{J_s}$ and surface magnetic current density $\mathbf{M_s}$ are given by

$$\mathbf{J_s} = \hat{n} \times \mathbf{H}, \quad \mathbf{M_s} = \mathbf{E} \times \hat{n}. \tag{A.2}$$

Via (A.1) and (A.2),

$$\mathbf{J_s} = \hat{z}I, \quad \mathbf{M_s} = -\hat{c}V. \tag{A.3}$$

We obtain node voltages and branch currents along the truncation boundary at discrete positions via circuit simulations. For the numerical calculations, current densities $\mathbf{J_s}$ and $\mathbf{M_s}$ are interpolated as

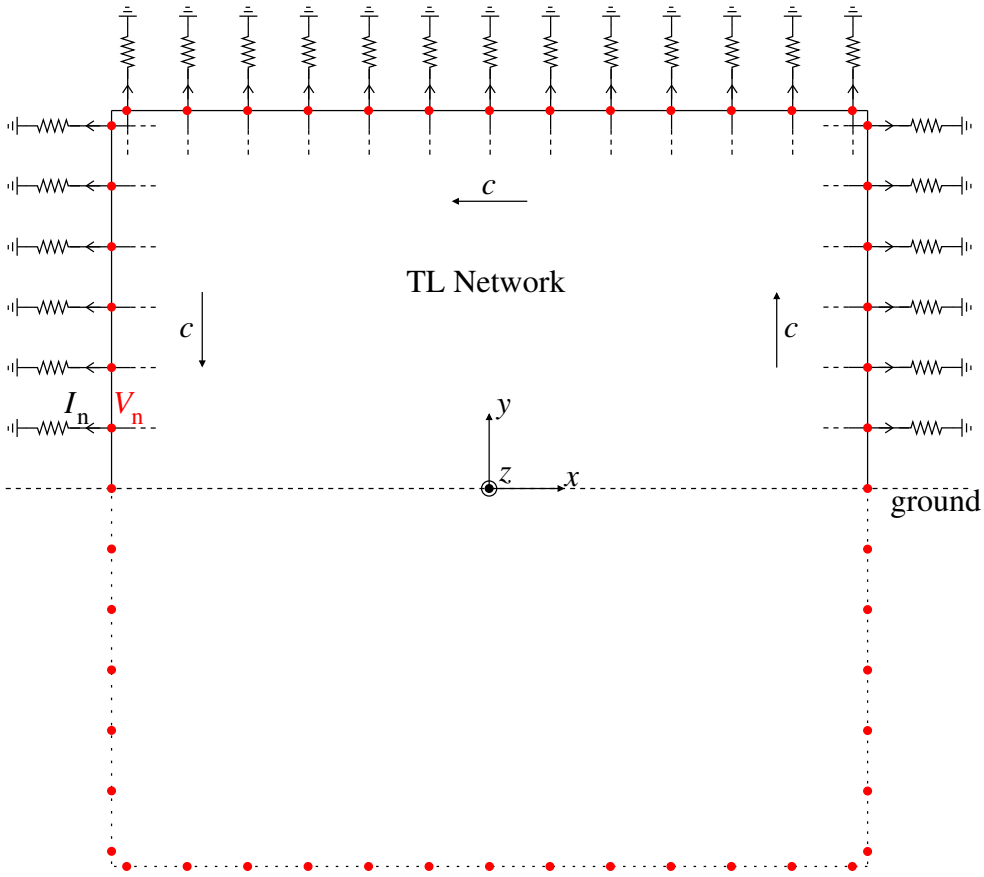

Figure A.1. Boundary node voltages and branch currents.

$$\mathbf{J_s} = \hat{z}\sum_{n=1}^{N} I_n f_n(\mathbf{r}'), \quad \mathbf{M_s} = -\hat{c}\sum_{n=1}^{N} V_n f_n(\mathbf{r}'), \tag{A.4}$$

where $f_n(\mathbf{r}')$ is a triangular interpolating function as shown in Figure A.2. In (A.4), V_n is the node voltage of node n and I_n is the branch current of the associated branch as indicated in Figure A.1. $\mathbf{r}'_\mathbf{n}$ is the position vector of node n and N is the total number of node voltage and branch current pairs.

Now, we apply the image theory by removing the ground plane and placing equivalent current densities in $y \leq 0$ along the dotted line indicated in Figure A.1. We consider the radiation of the original and the image current densities in free space. The radiation integrals $\mathbf{N}$ and $\mathbf{L}$ are defined to be

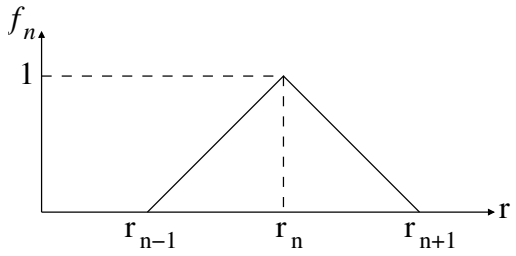

Figure A.2. Interpolation function.

$$\mathbf{N} = \int_C \mathbf{J} e^{jk\hat{r}\cdot\mathbf{r}'} dl', \quad \mathbf{L} = \int_C \mathbf{M} e^{jk\hat{r}\cdot\mathbf{r}'} dl', \tag{A.5}$$

where C is the closed contour composed of the original and the image boundaries. At far-field, the equivalent electric field expression can be written as [30]

$$\mathbf{E} = jkZ_0 \frac{e^{-jkr}}{\sqrt{jk8\pi r}} \left[\hat{r} \times \hat{r} \times \mathbf{N} + \frac{1}{Z_0} \hat{r} \times \mathbf{L} \right] \tag{A.6}$$

expressed in the cylindrical coordinate system (r, ϕ, z). Z_0 is the characteristic impedance of the TL grid which is the circuit equivalent for the intrinsic impedance of the free space. Using the field expression in (A.6), the far-field radiation pattern can be found. Finally, the directivity expression is given by

$$D(\phi) = \frac{U(\phi)}{2\pi \int_0^{\pi} U(\phi) d\phi}, \tag{A.7}$$

where

$$U = \frac{|E|^2}{2Z_0} \tag{A.8}$$

is the radiation intensity.

BIBLIOGRAPHY

[1] J. B. Pendry, D. Schurig, and D. R. Smith, "Controlling electromagnetic fields," *Science*, vol. 312, pp. 1780–1782, 2006.

[2] A. J. Ward and J. B. Pendry, "Refraction and geometry in Maxwell's equations," *J. Mod. Opt.*, vol. 43, no. 4, pp. 773–793, 1996.

[3] D. Schurig, J. J. Mock, B. J. Justice, S. A. Cummer, J. B. Pendry, A. F. Starr, and D. R. Smith, "Metamaterial electromagnetic cloak at microwave frequencies," *Science*, vol. 314, pp. 977–980, 2006.

[4] M. Rahm, S. A. Cummer, D. Schurig, J. B. Pendry, and D. R. Smith, "Optical design of reflectionless complex media by finite embedded coordinate transformations," *Phys. Rev. Lett.*, vol. 100, pp. 063 903/1–4, 2008.

[5] D.-H. Kwon and D. H. Werner, "Transformation electromagnetics: an overview of the theory and applications," *IEEE Antennas Propag. Mag.*, vol. 52, no. 1, pp. 24–46, Feb. 2010.

[6] H. Chen, C. T. Chan, and P. Sheng, "Transformation optics and metamaterials," *Nature Mater.*, vol. 9, pp. 387–396, May 2010.

[7] J. B. Pendry, "Negative refraction makes a perfect lens," *Phys. Rev. Lett.*, vol. 85, pp. 3966–3969, 2000.

[8] U. Leonhardt and T. G. Philbin, "General relativity in electrical engineering," *New J. Phys.*, vol. 8, pp. 247/1–18, 2006.

[9] S. A. Cummer, N. Kundtz, and B.-I. Popa, "Electromagnetic surface and line sources under coordinate transformations," *Phys. Rev. A*, vol. 80, no. 3, pp. 033 820/1–7, Sep. 2009.

[10] B.-I. Popa, J. Allen, and S. A. Cummer, "Conformal array design with transformation electromagnetics," *Appl. Phys. Lett.*, vol. 94, pp. 244 102/1–3, 2009.

[11] Y. Luo, J. Zhang, H. Chen, J. Huangfu, and L. Ran, "High-directivity antenna with small antenna aperture," *Appl. Phys. Lett.*, vol. 95, pp. 193 506/1–3, 2009.

[12] D.-H. Kwon and C. D. Emiroglu, "Low-profile embedded design of endfire scanning arrays with coordinate transformations," *J. Appl. Phys.*, vol. 107, pp. 034 508/1–8, 2010.

[13] D.-H. Kwon, "Transformation electromagnetic design of embedded monopole in a ground recess for conformal applications," *IEEE Antennas Wireless Propag. Lett.*, vol. 9, pp. 432–435, 2010.

[14] C. Caloz and T. Itoh, *Electromagnetic Metamaterials: Transmission Line Theory and Microwave Applications*. Hoboken, NJ: Wiley-IEEE Press, 2006.

[15] G. V. Eleftheriades and K. G. Balmain, *Negative Refraction Metamaterials: Fundamental Principles and Applications*. Hoboken, NJ: Wiley-IEEE Press, 2005.

[16] X. Liu, C. Li, K. Yao, X. Meng, and F. Li, "Invisibility cloaks modeled by anisotropic metamaterials based on inductor-capacitor networks," *IEEE Antennas Wireless Propag. Lett.*, vol. 8, pp. 1154–1157, 2009.

[17] G. Gok and A. Grbic, "Tensor transmission-line metamaterials," *IEEE Trans. Antennas Propag.*, vol. 58, no. 5, pp. 1559–1566, May 2010.

[18] M. N. Afsar, Y. Wang, and H. Ding, "A new wideband cavity-backed spiral antenna," *Proc. IEEE Antennas and Propagation Society Int. Symp.*, vol. 4, pp. 124–127, Jul. 2001.

[19] A. T. Adams, "Flush mounted rectangular cavity slot antennas–theory and design," *IEEE Trans. Antennas Propag.*, vol. 15, no. 3, pp. 342–351, May 1967.

[20] S. A. Long, "Experimental study of the impedance of cavity-backed slot antennas," *IEEE Trans. Antennas Propag.*, vol. 23, no. 1, pp. 1–7, Jan. 1975.

[21] C. R. Cockrell, "The input admittance of the rectangular cavity-backed slot antenna," *IEEE Trans. Antennas Propag.*, vol. 24, no. 3, pp. 288–294, May 1976.

[22] J. Hirokawa, H. Arai, and N. Goto, "Cavity backed wide slot antenna," *Proc. Inst. Elect. Eng.*, vol. 136, no. 1, pp. 29–33, Feb. 1989.

[23] H. Nakano, M. Iwatsuki, M. Sakurai, and J. Yamauchi, "A cavity-backed rectangular aperture antenna with application to a tilted fan beam array antenna," *IEEE Trans. Antennas Propag.*, vol. 51, no. 4, pp. 712–718, Apr. 2003.

[24] D. Schurig, J. B. Pendry, and D. R. Smith, "Calculation of material properties and ray tracing in transformation media," *Opt. Express*, vol. 14, pp. 9794–9804, 2006.

[25] D. R. Smith, D. Schurig, M. Rosenbluth, S. Schultz, S. A. Ramakrishna, and J. B. Pendry, "Limitations on subdiffraction imaging with a negative refractive index slab," *Appl. Phys. Lett.*, vol. 82, pp. 1506–1508, 2003.

[26] D.-H. Kwon and C. D. Emiroglu, "Non-orthogonal grids in two-dimensional transmission-line metamaterials," *IEEE Trans. Antennas Propag.*, submitted.

[27] C. Christopoulos, *The Transmission-Line Modeling Method TLM*. Piscataway, NJ: IEEE Press, 1995.

[28] C. R. Brewitt-Taylor and P. B. Johns, "On the construction and numerical solution of transmission-line and lumped network models of Maxwell's equations," *Int. J. Numer. Meth. Eng.*, vol. 15, pp. 13–30, 1980.

[29] A. Grbic and G. V. Eleftheriades, "Periodic analysis of 2-D negative refractive index transmission line structure," *IEEE Trans. Antennas Propag.*, vol. 51, pp. 2604–2611, Oct. 2003.

[30] R. F. Harrington, *Time-Harmonic Electromagnetic Fields*. Piscataway, NJ: IEEE Press, 2001.